AGU100 ADVANCING EARTH AND SPACE SCIENCE

JAMES | Journal of Advances in Modeling Earth Systems

RESEARCH ARTICLE
10.1029/2019MS001654

Key Points:
- A new framework to validate climate models and compare reanalyses products is presented
- We identify biases in the CESM Large Ensemble in relation to tropical teleconnections in SST
- We investigate the time evolution of ENSO variability in observational data sets and CESM Large Ensemble

Correspondence to:
F. Falasca,
fabrifalasca@gatech.edu

Citation:
Falasca, F., Bracco, A., Nenes, A., & Fountalis, I. (2019). Dimensionality reduction and network inference for climate data using δ-MAPS: Application to the CESM Large Ensemble sea surface temperature. *Journal of Advances in Modeling Earth Systems*, *11*, 1479–1515. https://doi.org/10.1029/2019MS001654

Received 11 FEB 2019
Accepted 13 APR 2019
Accepted article online 22 APR 2019
Published online 4 JUN 2019

Dimensionality Reduction and Network Inference for Climate Data Using δ-MAPS: Application to the CESM Large Ensemble Sea Surface Temperature

Fabrizio Falasca[1], Annalisa Bracco[1,2], Athanasios Nenes[1,3,4,5], and Ilias Fountalis[6]

[1]School of Earth & Atmospheric Sciences, Georgia Institute of Technology, Atlanta, GA, USA, [2]Institute of Geosciences and Earth Resources, National Research Council of Italy, Pisa, Italy, [3]ENAC, École Polytechnique Fédérale de Lausanne, Lausanne, Switzerland, [4]Institute of Chemical Engineering Sciences, Foundation for Research and Technology Hellas, Patras, Greece, [5]Institute for Environmental Research and Sustainable Development, National Observatory of Athens, P. Penteli, Greece, [6]College of Computing, Georgia Institute of Technology, Atlanta, GA, USA

Abstract A framework for analyzing and benchmarking climate model outputs is built upon δ-MAPS, a recently developed complex network analysis method. The framework allows for the possibility of highlighting quantifiable topological differences across data sets, capturing the magnitude of interactions including lagged relationships and quantifying the modeled internal variability, changes in domains properties and in their connections over space and time. A set of four metrics is proposed to assess and compare the modeled domains shapes, strengths, and connectivity patterns. δ-MAPS is applied to investigate the topological properties of sea surface temperature from observational data sets and in a subset of the Community Earth System Model (CESM) Large Ensemble focusing on the past 35 years and over the 20th and 21st centuries. Model ensemble members are mapped in a reduced metric space to quantify internal variability and average model error. It is found that network properties are on average robust whenever individual member or ensemble trends are removed. The assessment identifies biases in the CESM representation of the connectivity patterns that stem from too strong autocorrelations of domains signals and from the overestimation of the El Niño–Southern Oscillation amplitude and its thermodynamic feedback onto the tropical band in most members.

1. Introduction

Earth's climate exhibits a range of recurrent spatiotemporal patterns ("modes of variability") that interact with each other on several spatial and time scales. Their investigation is inherently challenging, but may be greatly aided by Knowledge-Discovery through Data-mining methodologies (Fayyad et al., 1996). Complex network analysis characterizes the topological properties of a given (climate) field by identifying sets of nodes that dominate the exchange of information across the system and by quantifying their connections, so-called "links" or "edges" (Barabási, 2016; Newman, 2010). In the context of climate science, nodes usually represent geographical locations, while links capture local or nonlocal interactions ("teleconnections") among them.

Applications of complex network analysis to climate science dates back to 2004, when Tsonis and Roebber (2004) applied graph theory to the analysis of global geopotential height data. Since then, many studies based on network analysis focused on topics ranging from the prediction of El Niño episodes (Ludescher et al., 2013) and its influence on global scale (Wang et al., 2009; Yamasaki et al., 2008), to the importance of Rossby waves in the transport of information around the globe (Wang et al., 2013). Attempts to switch from correlation-based networks to causal ones have been made by Runge et al. (2015), Ebert-Uphoff and Deng (2017), and Hlinka et al. (2017), and methodologies have been proposed to study nonlinear interactions (Donges et al., 2009a).

In climate network analysis, the standard approach is to construct networks using gridded data and considering each grid cell as a node. Two nodes are connected if some measure (such as Pearson correlation and mutual information) is found greater than a preselected value; otherwise, the link is pruned. However, cell-level pruning causes a loss of robustness in the final network, so that slightly different data sets, for example different reanalyses of the same climate field, may produce significantly different links, limiting

the applicability of cell-pruning methods to intercomparison studies (Fountalis et al., 2014, 2015). Community detection and clustering algorithms have also been used for dimensionality reduction purposes (Kawale et al., 2011, 2012; Steinhaeuser et al., 2010), but they usually do not include information about the sign of the links or their relative importance. Moreover, these algorithms may identify clusters that are not spatially contiguous and typically not overlapping.

Here we introduce and apply to the analysis of climate fields a recently developed network methodology named δ-MAPS (Fountalis et al., 2018) able to characterize connectivity patterns in highly complex spatiotemporal systems and compare them in different data sets without the above limitations. δ-MAPS identifies the underlying fundamental components (referred to as "domains") of a spatiotemporal system, and their links. Domains are represented as potentially overlapping, spatially contiguous regions characterized by highly correlated temporal activity. A weighted and potentially directed network is then inferred between domains: the weights take into account the magnitude and sign of the interactions and the link direction takes into account the temporal ordering of events. An important characteristic of climate time series is the presence of strong autocorrelations (Guez et al., 2014) that require separation from dynamical links. δ-MAPS accounts for this problem in the network inference process using the appropriate statistic.

Our goal here is to present this methodology and one possible application to the analysis of climate fields, and unveil the network structure of sea surface temperature (SST) in two data sets (HadISST, Rayner et al., 2003; and COBEv2, Hirahara et al., 2014) and in 30 members of the Community Earth System Model Large Ensemble (CESM-LE) (Kay et al., 2015). Attention is given to differences between modeled and observed networks stemming from model biases and internal variability of the system. We also investigate changes in the modeled climate networks as a function of the detrending method. The analysis spans first 35 years, from 1980 to 2015, and then expands to 1920–2100 for some of the model integrations, with a focus on the evolution of the tropical domains. Four metrics, one developed by the authors (netCorr), and three adopted from the network analysis literature, aid the comparison, allowing to quantify similarities and differences across all SST networks and the internal variability of the CESM ensemble.

The paper is organized as follows. Section 2 describes δ-MAPS and the metrics adopted: Normalized Mutual Information (NMI; McDaid et al., 2013), domain strength and signal (Fountalis et al., 2018), Similarity (S) built upon Fountalis et al. (2015) and the new netCorr metric. The different data sets analyzed are introduced in section 3. The SST network in the two observational data sets is then presented (section 4). In sections 5–7 we evaluate the network structure of 30 members of the CESM-LE. Section 8 focuses on the temporal evolution from 1920 to 2100. Summary and discussion conclude the work.

2. Methodology

A detailed description of δ-MAPS is given in Fountalis et al. (2018). We note that δ-MAPS differs from the method developed in Fountalis et al. (2014), while building on similar premises, and is therefore a distinct methodology requiring different metrics. As mentioned in Fountalis et al. (2018), δ-MAPS provides a dimensionality reduction strategy and it is similar, in its main objective, to other clustering, network community detection, functional network inference, or multivariate statistical methods. Among those, Principal Component (PC) or Empirical Orthogonal Function (EOF) methods are widely used in climate science. Using synthetic data, Fountalis et al. (2018) have shown that δ-MAPS is advantageous, compared to EOF and several other reduction algorithms such as clustering, community detection, or Independent Component Analysis, for identifying the distinct semiautonomous components of a spatiotemporal system and to infer their (potentially lagged and weighted) connections. Here we present briefly the methodology and, in details, the metrics—not discussed in Fountalis et al. (2018)—with the specific aim of climate applications, and we summarize the outcomes of the comparison of δ-MAPS and other reduction methodologies.

2.1. δ-MAPS

δ-MAPS is a network analysis method suitable for the investigation of spatiotemporal data sets. First, δ-MAPS identifies the underlying components in a spatiotemporal system, which we refer to as *domains*; domains are spatially contiguous, possibly overlapping, functionally homogeneous sets of grid cells. Then it infers a functional network between the identified domains, represented as a weighted and directed graph. The weight of a link captures the magnitude of the interaction between two domains; links can have either positive or negative weights, and the sign of a link captures different types of interactions. Each link has also

a time lag or a range of time lags; these lags determine link direction and give information about the temporal ordering of events. In the following we describe the two stages of δ-MAPS, namely, domain identification and network inference.

The δ-MAPS software can be obtained in https://github.com/FabriFalasca/delta-MAPS.

2.1.1. Domain Identification

A *domain* is a spatially contiguous region whose grid cells somehow participate in the same dynamic effect or function. It follows that domains should have epicenters or cores where the local homogeneity is maximum. The first step is therefore to identify such cores, and the second is to expand those cores to identify the full extent of a domain.

More formally, each grid cell i is associated with a time series $x_i(t)$ of length T. Linear trends are removed from the time series using a least squares fit. We verified that using the Theil-Sen estimator for trend removal (as done in Fountalis et al., 2015) to reduce sensitivity to outliers does not affect the results. We assume that $x_i(t)$ is stationary, and we denote its mean and variance as $\hat{\mu}_i$ and $\hat{\sigma}_i^2$, respectively. The similarity between the functional activity of two grid cells i and j is then captured by the Pearson correlation at zero lag (but any other correlation measure could be used instead):

$$r_{i,j} = \frac{\sum_{t=1}^{T}(x_i(t) - \hat{\mu}_i)(x_j(t) - \hat{\mu}_j)}{T\sqrt{\hat{\sigma}_i^2\hat{\sigma}_j^2}}. \tag{1}$$

To identify the cores of the spatiotemporal field, we first construct a local homogeneity field that captures the similarity between the time series of any given grid cell with its spatial neighbors by defining the K neighborhood of a grid cell i, $\Gamma_K(i)$, that includes the grid cell i and its K nearest neighbors according to an appropriate distance metric (here geodesic distance). The local homogeneity at cell i is defined as the average pairwise correlation of the cells in $\Gamma_K(i)$

$$r_K(i) = \frac{\sum_{m\neq n\in\Gamma_K(i)} r_{m,n}}{K(K+1)}. \tag{2}$$

We will use a similar notation for the homogeneity of a set of grid cells A

$$r(A) = \frac{\sum_{m\neq n\in A} r_{m,n}}{|A|(|A|+1)}, \tag{3}$$

with $|A|$ being the cardinality of the set.

We then identify the cores such that $r_K(i)$ is a local maximum and is larger than a predetermined threshold δ. Therefore, a grid cell i is a core if $r_K(i) > \delta$ and $r_K(i) > r_K(j), j \neq i, \forall j \in \Gamma_K(i)$.

Cores are then iteratively expanded and merged to identify domains. The total number of domains, denoted by m, depends on δ, and their minimum size is set by K. Domains are spatially contiguous, might overlap and might include more than one core. Also, grid cells may not belong to any domain.

The proposed domain identification relies on two parameters, the neighborhood size K and the threshold δ. As K decreases, the local homogeneity field becomes noisier and the number of core grid cells increases; as K increases, the local homogeneity field becomes smoother, removing seeds and potentially hiding domains. In section A.1 we propose a heuristic to select the "optimal" K. δ is the minimum degree of homogeneity required for a set of grid cells to form a domain and affects both the number of core grid cells and the size of the domains. The larger is δ, the fewer cores are identified, and the larger are the domains. A statistically based heuristic to select δ is proposed in section A.2.

2.1.2. Network Inference

Once m domains are identified, a *functional* network is constructed among them. To this end, for each domain a signal $X_A(t)$ is defined as the cumulative anomaly of the grid cells over the domain's scope such that

$$X_A(t) = \sum_{i=1}^{|A|} x_i(t)\cos(\phi_i), \tag{4}$$

with ϕ_i being the latitude of grid cell i.

The correlations over a lag range $-\tau_{\max} \leq \tau \leq \tau_{\max}$ between any two domains A and B are then estimated as

$$r_{A,B}(\tau) = \frac{\sum_{t=1}^{T-\tau}(X_A(t) - \hat{\mu_A})(X_B(t+\tau) - \hat{\mu_B})}{T\sqrt{\hat{\sigma}_A^2 \hat{\sigma}_B^2}}. \quad (5)$$

The next step is to examine the statistical significance of the $2 \times \tau_{\max} + 1$ correlations between each domain pair A and B.

Given that two uncorrelated signals can still produce significant correlations if they have a strong autocorrelation structure, we choose a statistical significance test that accounts for autocorrelations and adopt the Bartlett's formula (Box et al., 2011).

Two domains, A and B, are connected with a link if there exists at least one significant correlation at lag $\tau \in [-\tau_{\max}, \tau_{\max}]$. If two or more significant correlations exist, then a link may be associated with more than one lag value. Specifically, we first consider the lag value τ^* that maximizes the correlation in absolute sense and denote $r^*_{A,B}$ as the corresponding correlation. We then associate to each link the range of lags $R_{A,B}(\tau)$ that (a) have significant correlations and (b) are within 1 STD (computed by the Bartlett's formula) from $|r^*_{A,B}|$. If $R_{A,B}(\tau)$ includes the zero lag, then the link between A and B is undirected. If $R_{A,B}(\tau)$ has strictly positive lags, then a directed link is formed and domain A is a temporal predecessor of domain B. If $R_{A,B}(\tau)$ is strictly negative, the link is directed and A is a temporal successor of B. We emphasize that link direction does not imply causality, but simply temporal ordering.

Finally, a weight is assigned to each link to capture the magnitude of the interactions between domains. To account for the signal strength of each domain, the weight of a link is computed as the covariance between the signals of domains A and B

$$w(A,B) = \mathrm{Cov}[X_A(t), X_B(t)] = \sqrt{\hat{\sigma}_A^2 \hat{\sigma}_B^2} r^*_{A,B}. \quad (6)$$

Link weights can be positive or negative, depending on the sign of $r^*_{A,B}$, representing different functional relationships between two domains. Instead of $r^*_{A,B}$, an average correlation value could be adopted instead.

Every network presented in this work has been inferred using monthly time series and $\tau_{\max} = 12$ months.

2.2. Metrics

We propose a set of four metrics to ensure a comprehensive comparison between networks: the NMI that quantifies similarities and differences in shape and size of domains, the domain strength that establishes the relative importance of a domain in the network, the Similarity metric that quantifies the distance of two networks in terms of their domains' strength, and the newly developed netCorr that estimates differences in the topology of two networks.

2.2.1. Normalized Mutual Information

The NMI is well known in the network literature (Lancichinetti et al., 2009; McDaid et al., 2013). Within the δ-MAPS framework the NMI quantifies the similarity of two networks N_1 and N_2 in terms of their domains. This metric accounts for the possibility that domains may overlap, and it is therefore chosen against the adjusted rand index (Hubert & Arabie, 1985; Steinhaeuser et al., 2012) adopted in Fountalis et al. (2014, 2015).

It is calculated by assigning a label to each grid point in the data sets under investigation as function of the domains it belongs to, generating a probability distribution that a randomly selected node may belong to a domain D in each network, $P(D_{N_1})$ and $P(D_{N_2})$, along with the joint probability $P(D_{N_1}, D_{N_2})$ and finally defining the mutual information as

$$\mathrm{MI} = \sum_{D_{N_1}, D_{N_2}} P(D_{N_1}, D_{N_2}) \log_2 \frac{P(D_{N_1}, D_{N_2})}{P(D_{N_1})P(D_{N_2})}. \quad (7)$$

Every pair of grid points that belong to the same domain(s) in both partitions contributes positively to the MI, and vice versa for any pair of nodes that belong to one or more domain in one partition, but to different ones in the other network. The NMI is the normalized version of the MI in equation (7) so that it varies between 0 (complete disagreement between the domains of the two networks) to 1 (identical set of domains). Different normalizations have been proposed in the literature; here we adopted the algorithm proposed by McDaid et al. (2013).

2.2.2. Domain Strength

The link weight w between any two domains is computed as the covariance between their respective domain signals (see equation (6)). Given a network N, the strength $s_N(A)$ of domain A is then defined as the sum of the absolute weights w of all links of that domain as

$$s_N(A) = \sum_i |w_i|. \tag{8}$$

The strength of a domain ignores link direction and intuitively informs about its relative importance in establishing the connectivity pattern of the network.

2.2.3. Similarity

Building upon the Distance metric proposed in Fountalis et al. (2015), we adopt a Similarity metric, "S," to compare two networks in terms of their domains' strength.

For a given field, a set of identified domains along with their respective strengths defines its strength map (i.e., see Figure 1). Every grid point i is associated to the value 0 if it does not belong to any domain, or to the strength s if it belongs to a domain with strength s. Whenever the grid cell belongs to two or more domains with different strength values, the highest is chosen. Following Fountalis et al. (2015) given two networks N_1 and N_2 their Distance "D" is defined as

$$D(N_1, N_2) = \frac{\sum_{i=1}^{n} |s_{N_1}(i) - s_{N_2}(i)|}{\sum_{i=1}^{n} |s_{\hat{N_1}}(i) - s_{\hat{N_2}}(i)|}. \tag{9}$$

Here n is the number of nonmasked grid points (grid cells in the ocean in the case of SSTs); $s_{N_1}(i)$ is the strength assigned to the grid cell i in the the network N_1 and similarly for $s_{N_2}(i)$. The network $\hat{N}$ is a randomized instance of network N in which the grid points have been randomly permuted on the underlying grid.

If $D(N_1, N_2) = 0$, then there is complete agreement between N_1 and N_2 in terms of domains strengths and vice versa if $D(N_1, N_2) \sim 1$.

S is simply defined as

$$S(N_1, N_2) = 1 - D(N_1, N_2), \tag{10}$$

so that $S(N_1, N_2) \sim 0$ represents a complete disagreement in domains' strengths between N_1 and N_2 and vice versa for $S(N_1, N_2) = 1$.

2.2.4. netCorr

$S(N_1, N_2)$ enables the comparison of two networks in terms of the strength of their domains; however, it does not quantify differences in their network structure (topology). Colocated domains in two different networks could have similar strengths but different connectivity patterns and, therefore, a different topological role. Here we propose a new metric, named "netCorr," that evaluates the connectivity pattern between all domains, expressed through an adjacency matrix, and compares it between networks.

Given a data set with n nonmasked grid points and its network N, the adjacency matrix M_N element (k, l) encodes the links of the domains as follows:

1. If the grid point k does not belong to any domain d_i, then it is not playing any role in the climate network and its connectivity is zero. A value of zero is given to all entries in the kth row of the matrix M_N;
2. If k belongs to a domain d_i, its relation with another grid point l is described by one of the following:
   - If the grid point l does not belong to any domain or if it belongs to a domain not connected to d_i, then the element (k, l) is zero;

- If l belongs to a domain d_j connected to d_i with a correlation $r^*_{i,j}$, then the value of $r^*_{i,j}$ is assigned to the position (k, l) whenever the link is such that $d_i \rightarrow d_j$ (d_i is leading d_j) or $d_i \leftrightarrow d_j$ (their lag range include zero). In the case of d_j overlapping with one or more domains also connected to d_i, the chosen value for the element (k, l) is the one that maximizes the correlation in its absolute value. The metric therefore records the strongest connections (positive or negative). Additionally,
- if l belongs to a domain d_j connected to d_i with a correlation $r^*_{i,j}$, but $d_i \leftarrow d_j$ (d_i is led by d_j), then $(k, l) = 0$. With this choice the metric tracks the temporal ordering of the network.

3. If k belongs to two (or more) overlapping domains d_i and d_j, we consider it as belonging to the strongest one and proceed as described for k belonging to one domain. The element (k, k), however, is a nonzero entry and contains the value of the connection that the strongest domain has with the one it is overlapping with. In the case of multiple overlappings, the element (k, k) will be set equal to the largest correlation in absolute sense.

Given two networks N_1 and N_2 we then define netCorr as the two-dimensional correlation between their matrices M_{N_1} and M_{N_2}:

$$\text{netCorr} = \text{Corr}[M_{N_1}, M_{N_2}]. \tag{11}$$

The computation of the netCorr using synthetic data is exemplified in Appendix B.

2.2.5. Comparison With Other Methods

The δ-MAPS presents several advantages against existing approaches for dimensionality reduction and network inference. Here we present a brief summary; an extensive, quantitative comparison based on synthetic data is presented in Fountalis et al. (2018).

The most popular approach to dimensionality reduction in climate science is PC or EOF analysis. For a given data set, EOFs are defined as the eigenvectors of the covariance matrix and they define patterns, by definition orthogonal to each other, where most of the variance is concentrated. The eigenvalues of the matrix (PCs) define the variability in time of their corresponding EOF. The orthogonality constraint, however, complicates the interpretation of the results making it difficult to distinguish a physical mode from a purely statistical one (Dommenget & Latif, 2002). To overcome this issue, it is common to rotate the EOFs, but this is sensitive to the rotation criterion, number of rotated EOFs, and their normalization (Tantet & Dijkstra, 2014; von Storch & Zwiers, 2001). The domains identified by δ-MAPS, on the other hand, are not subject to orthogonal constraints, and the components with low variance are not masked (Fountalis et al., 2018). EOFs cannot identify functional components that have lagged interactions, but a climate mode can play an important role in the connectivity pattern of the system while having a statistically nonsignificant variance at lag $\tau = 0$.

Given the known drawbacks of PC analysis, in recent years several methods based on unsupervised clustering have been proposed for dimensionality reduction purposes (Baldassano et al., 2015; Blumensath et al., 2012; Craddock et al., 2012; Fountalis et al., 2014; Heuvel et al., 2008; Kawale et al., 2013; Lu et al., 2003; Thirion et al., 2014). These algorithms have the following in common: the identified clusters may not be spatially contiguous, almost every grid cell must belong to a cluster, and in most cases the number of clusters is an input parameter. Moreover, none of these methods accounts for spatial overlapping. The common approach when inferring a climate network is to consider grid points as nodes of a spatially embedded graph (Donges et al., 2009b; Feng & Dijkstra, 2016; Kittel et al., 2017; Ludescher et al., 2013; Tsonis & Roebber, 2004; Wang et al., 2009, 2013; Yamasaki et al., 2008). This is a powerful approach, but less useful for intramodel or intermodel comparison purposes since grid cells are not distinct semiautonomous components of the underlying system. Another method consists in inferring networks using known climate indices as nodes (Swanson & Tsonis, 2009; Tsonis et al., 2007; Wang et al., 2009), but it cannot be used to identify unknown spatiotemporal patterns of climatic relevance and has limitations if applied to (imperfect) models whenever the indices are derived from the observed system.

At least three frameworks stemming from network analysis and different from δ-MAPS have been proposed in the recent literature for model intercomparison purposes (Feldhoff et al., 2014; Steinhaeuser & Tsonis, 2014; Tantet & Dijkstra, 2014). Feldhoff et al. (2014) construct a cell-level network and apply it to evaluate the performance of two regional models in representing South American climate. They compute all pairwise correlations between grid cells and retain only the positive values. The network is then represented as a

binary graph, where correlations below a certain fixed threshold are pruned. Steinhaeuser and Tsonis (2014) evaluate an ensemble of CMIP3 models inferring networks by computing correlations at zero lag between all grid cells; correlations with absolute value less than 0.5 are pruned. The network is then represented as a binary graph, used as input for a community detection algorithm (Clauset et al., 2004), and model outputs are compared in terms of their community structure. A similar approach is proposed also in Tantet and Dijkstra (2014), where the structure of the identified communities is then investigated in terms of the spatiotemporal variability of the observed SST field. All three methodologies are limited in their applicability by the pruning at the cell level and/or by the selection of correlations of a given sign, as shown in detail in Fountalis et al. (2014, 2015).

Given the objective of this work, that is, to compare climate models and observational data sets both on the level of spatial representation of modes of variability and their connectivity patterns, δ-MAPS presents several advantages. They can be summarized as follows: (i) the possibility to infer a weighted and eventually directed network, where link weights and their directionality quantify the magnitude and temporal ordering of climate teleconnections; (ii) the definition of positive and negative links, so that functional relationships in the system are preserved and considered; and (iii) the domain identification method that separates communities that are not spatially contiguous and have different roles in the global climate system, which is not achieved by most community detection algorithms (Fountalis et al., 2018 provides one such example).

3. Data Sets

In this work we analyze and compare networks of SST for two data sets, HadISST (Rayner et al., 2003) and COBEv2 (Hirahara et al., 2014), and 30 members of the CESM Large Ensemble (Kay et al., 2015). For the most part, data sets are analyzed at a resolution of $1.25° \times 1°$ and over the latitudinal range [60°S, 60°N] to avoid regions covered by sea ice in parts of the year. All networks are computed using linearly detrended monthly anomalies. We perform most analyses over the period 1980–2015 during which in situ SST measurements are integrated with satellites data. In section 8 we extend the analysis to 1920–2100 using, in the case of CESM, the historical integrations forced by best estimates of natural and anthropogenic contributions up to 2005, and then the integrations forced according to the concentration pathway 8.5 (RCP8.5; Kay et al., 2015).

Trend maps for COBEv2 and HadISST are shown later on (section 5). Here it is worth noting that patterns of warming and cooling are similar, but a stronger warming is found in COBEv2. Positive trends are found in the North Atlantic, Indian Ocean, and subtropical Pacific, with limited cooling mostly in the El Niño–Southern Oscillation (ENSO)-impacted area of the Tropical Pacific and in the Southern Ocean. The trend patterns during the satellite era are reminiscent of the "global warming pause" or "hiatus" observed between 1998 and 2012, and have been the subject of numerous investigations. Various causes have been proposed for such patterns, ranging from weaker than normal solar forcing, increased low level cloud coverage, large aerosol loadings and increased water vapor in response to increased CO_2 (Kaufmann et al., 2011; Lockwood, 2008; Medhaug et al., 2017; Regayre et al., 2014; Thorne et al., 2015; Zhou et al., 2016) to internal variability (Dai et al., 2015; Dong & Zhou, 2014; England et al., 2014; Kosaka & Xie, 2013; Mann et al., 2014; Yao et al., 2016). It is likely that a combination of multiple factors contributed to the observed spatial distribution of warming and cooling. The CESM ensemble allows us to unravel the internal variability component—under the assumption that the model is reasonably representing it—and investigate network differences as function of the removed trend. Additionally, we explore the link between ENSO and the tropical band and its representation in CESM using air temperature data from the model ensemble and from the MERRA-2 project (Molod et al., 2015).

4. The Observed SST Network

The SST strength maps for the observational data sets are presented in Figures 1a and 1c. Each domain is colored according to its strength. Strong domains are robustly identified with similar shape and size in both COBEv2 and HadISST and cover the ENSO region (E), the South (TA_S) and North Tropical Atlantic (TA_N), the Pacific horseshoe pattern area, with one branch extending from the South Pacific Convergence Zone through Indonesia (horseshoe pattern south HS_S) and the other from Indonesia northeastward into the North Pacific (horseshoe pattern north HS_N), the Indian Ocean (IO) and the South Eastern Pacific (SP). Similarities between weaker domains are also present, especially in the North Atlantic and around the Gulf

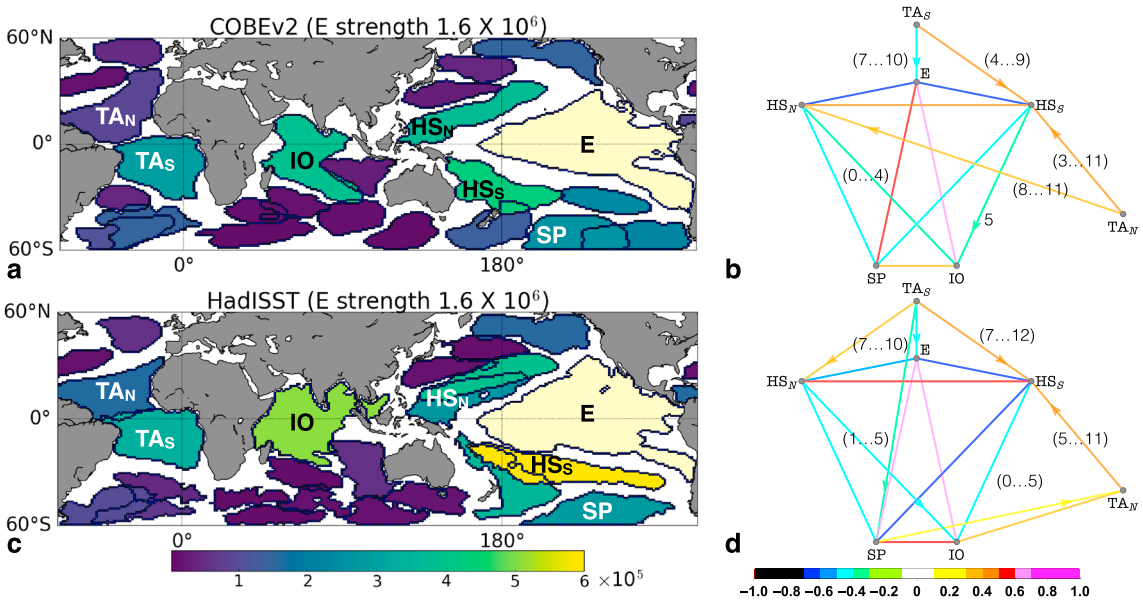

Figure 1. Strength maps for COBEv2 (a) and HadISST (c), and networks between seven strongest domains in COBEv2 (b) and HadISST (d). In panels (a) and (c), the strength of the *E* domain is reported atop of each panel. In panels (b) and (d) the color of the links quantifies the corresponding cross correlation and the arrows indicate the links' directionality. The lag ranges associated with some connections are also reported in the parenthesis. Lags are expressed in months.

Stream and the Kuroshio extension. Larger differences are found in the Southern Ocean, where the two datasets have low correlations.

Domains can exchange information through oceanic processes, atmospheric teleconnections, and coupled atmospheric-ocean dynamics. These exchanges result in complex connectivity patterns ("connections"), as shown in Figures 1b and 1d focusing on the links between the seven strongest domains for clarity. Connections to/from the *E* domain are captured with similar correlations and weights in the two data sets, and this translates in analogous value of *E* strength, 1.56×10^6 in HadISST and 1.61×10^6 in COBEv2. Generally, however, the domains in COBEv2 are slightly weaker than in HadISST. Given the similarities in shape and size of the domains, these differences arise primarily from the correlations between the domains signals. Few of the connections shown are lagged.

Known atmospheric teleconnections such as those between the *E* and the basin-wide Indian Ocean (*IO*) domains and the horseshoe pattern are captured (Alexander, 2002; Chowdary & Gnanaseelan, 2007; Klein et al., 1999); intense correlations are also found between the *E* and South Pacific (*SP*) domains. δ-MAPS identifies also a 7 to 10 months lead of the TA_S domain on *E*, in agreement with several recent studies (Ding et al., 2012; Ham et al., 2013; Keenlyside & Latif, 2007; Rodriguez-Fonseca et al., 2009; Wang et al., 2010), with maximum anticorrelation of ~ -0.46 in both HadISST and COBEv2. This lead originates from an atmospheric bridge linking the SST variability of the equatorial Atlantic with that in the eastern Pacific. As shown in Rodríguez-Fonseca et al. (2009), anomalous warming in the equatorial Atlantic locally enhances convective activity over the basin and atmospheric Rossby waves transfer the signal to the Pacific basin. The Rossby waves strengthen the upward branch of the Walker circulation cell in the Atlantic and induce surface divergence in the eastern/central Pacific. Consequently, the westward winds strengthen causing enhanced upwelling along the coast of South America. The outcome is cooler waters in the eastern Pacific and a reinforcement of the Bjerknes feedback favoring La Niña conditions. The opposite holds whenever the equatorial Atlantic is cooler than average.

Domains are homogeneous regions of the spatiotemporal field under study and their cells have a variability in time similar enough that the overall averaged correlation is greater than δ. The similarity between domains can be tested by looking not only at the shape and size of their respective domains but also at their signal, as shown in Figure 2 for three among the strongest domains (*E*, TA_N, and *IO*). The correlations between the respective domain signals is 0.98 for the *E* domain, 0.96 for the TA_N, and 0.91 for the *IO*. These high correlations, despite small but nonzero differences in shape and size of the domains, imply that domains embed regions where the signal originates that are smaller than their whole size. For example, in

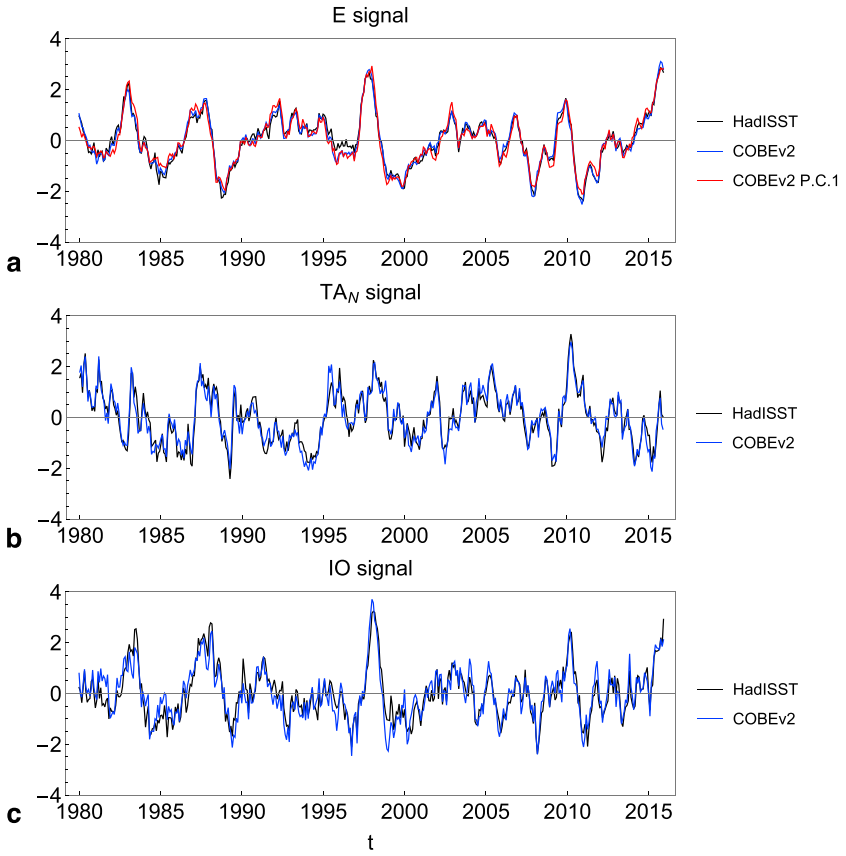

Figure 2. Signals (see equation (4) in the main text) of (a) the E, (b) the TA_N, and (c) IO domains, for the HadISST and COBEv2 at monthly resolution. All signals are normalized using their respective standard deviation. In (a), the first global PC for COBEv2 is also reported.

the E domain the dominant signal emerges from the equatorial band, in the TA_N from the tropics, and in the TA_S again from the equatorial region (Bracco et al., 2018).

Differences in the time variability of the domains are reflected in the network structure. For instance, a statistically significant link between TA_N and IO is found in HadISST and not in COBEv2 because correlations at lag 0 in the two data sets are 0.38 and 0.26, above and below the significance threshold, respectively. This translates in a similarly shaped correlograms of the TA_N and IO signals but in a statistical significance inferred only for HadISST.

For comparison purposes we computed the first three EOFs for the COBEv2 data set. The first EOF explains only ∼20.4% of the total variance, implying that the SST field is too complex to be described by the first mode. The second and third EOFs explain, respectively, the ∼7.4% and ∼4.4% of the total variance. Similarities between the EOF analysis and δ-MAPS are expected, and in Figure 2 the first PC in COBEv2 is plotted against the normalized E signals. The correlation between the first PC and the E signal is higher than 0.97 independently of the data set. Moreover, also the spatial pattern of the first EOF (not shown here, see Fountalis et al., 2018 or Tantet & Dijkstra, 2014) is well captured by the strong negative (positive) link weights between the E domain and domains in the Pacific horseshoe (Indian Ocean) regions. Therefore, the first EOF mode is essentially contained in our framework.

A key benefit of δ-MAPS, compared to EOF analysis or our previous network framework (Fountalis et al., 2014, 2015), stems from the inclusion of lagged relationships across domains. For example, the region corresponding to the TA_S domain has low variance in the principal components and was not captured in its link to ENSO by the previous network method (Fountalis et al., 2014, 2015), despite having a robust temporal leading on the strongest domain of the network.

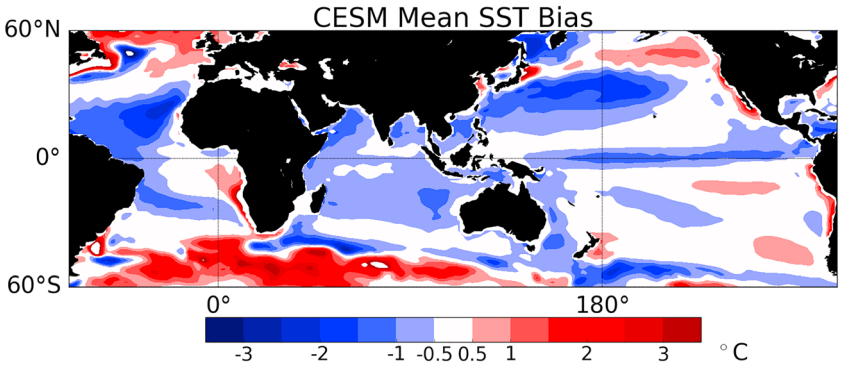

Figure 3. Mean sea surface temperature (SST) climatological bias computed against the COBEv2 data set (CESM-COBEv2) for the period 1980–2015. CESM = Community Earth System Model.

The identified domains in Figure 1 share qualitative similarities with the communities identified by Tantet and Dijkstra (2014). We emphasize that domains differ quantitatively from communities in terms of their spatial contiguity; moreover, connections between domains can be analyzed in terms of their sign, magnitude, and directionality.

5. CESM Climate Networks

Before delving in network analysis of the CESM-LE, we briefly present the model climatological biases and its linear trends (Figure 3).

The modeled climatologies are very similar across the ensemble, resulting in nearly identical maps across members over the period of interest. The modeled climatology is characterized by anomalously warm SSTs in the major upwelling systems (eastern boundaries and Southern Ocean), and in correspondence of the North Atlantic Current and Kuroshio extensions, and colder than observed SSTs in the equatorial Pacific, Indian Ocean, North Tropical, and Southern Western Atlantic.

Despite the similar climatologies, the runs differ substantially in their linear trends, with few members (8, 10, 14, and 25) reproducing several features of the observed one. In Figure 4 we show the linear trends for the two observational data sets and four different members (member 8, 12, 13, and 22), together with the ensemble mean trend and ensemble trend STD. Trend maps for all 30 runs are found in the appendix (Figure D1). In the observational data sets the trend patterns are similar but generally stronger in COBEv2 than in HadISST, reminiscent of a negative PDO signal in the Pacific and characterized by a widespread warming in the North Atlantic and in the Indian Ocean. Overall, linear trends in CESM appear closely related to dominant modes of variability, as to be expected given the length of the period considered. Differences between members and the ensemble trend STD (see Figure 4h) highlight the internal variability of the system (Deser et al., 2012). For example, members 8 and 13 have trends dominated by opposite phases of the PDO pattern, while member 12 displays a negative PDO pattern and warming in the equatorial Atlantic over the region of influence of the Atlantic Niño (Keenlyside & Latif, 2007; Zebiak, 1586). Member 22, on the other hand, is characterized by warming limited to the equatorial eastern Pacific and Kuroshio extension region, with a pattern similar to that of the ensemble mean trend, but more intense. Noticeably, none of the runs reproduces the observed cooling south of 50°S. The ensemble mean trend is characterized by a generalized warming except for the cold blob south of Greenland (Drijfhout et al., 2012; Rahmstorf et al., 2015) that is however absent in the observations. The warming is more intense in the equatorial Pacific, equatorial Atlantic, Kuroshio extension, southern Atlantic Ocean, the Indian Ocean along the African coast, and in the North Atlantic especially along the coast of Canada.

In the following we will explore the role that the variability in linear trend plays in determining the networks by presenting domains and their connections whenever individual trends or the ensemble mean trend are removed using the metrics introduced earlier: NMI, strength, S, and netCorr. The ensemble mean trend represents the forced component linked to increased concentrations of greenhouse gases under the assumption that 30 members are sufficient to sample the internal variability of the system.

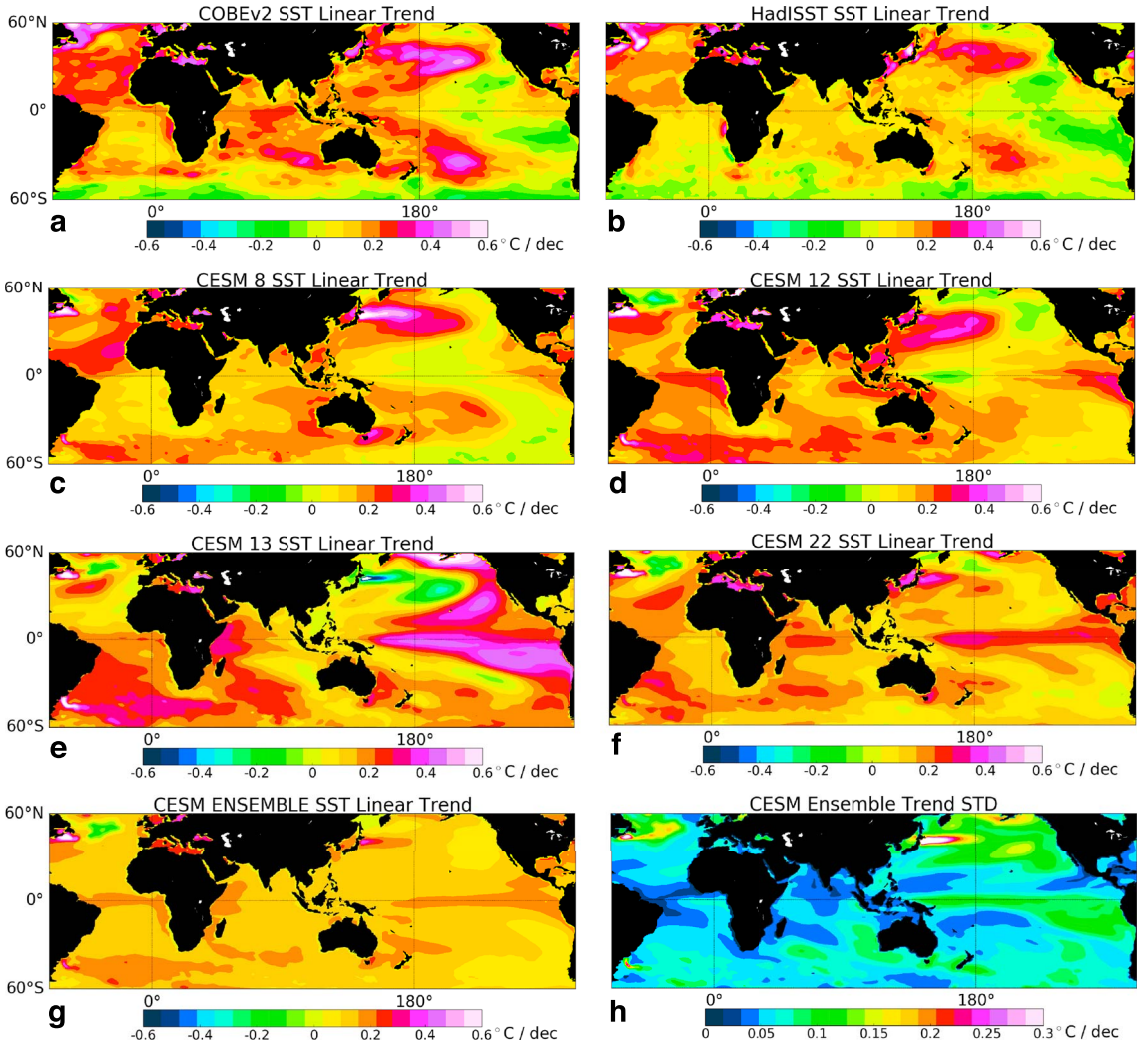

Figure 4. Linear trends for the period 1980–2015 in COBEv2 (a), HadISST (b), and members 8, 12, 13, and 22 (c–f). Ensemble mean trend (*g*) and ensemble mean standard deviation (*h*). SST = sea surface temperature; CESM = Community Earth System Model.

In Figure 5 the strength maps for the four members (8, 12, 13, and 22) are shown after removing the individual or the ensemble mean trends (maps for all ensemble members are presented in the appendix, in Figures C1 and C2). Independently of the trend removal, the strongest domain is always *E*. Its shape varies from being equatorially confined, as in the case of member 12, to resembling more closely the PDO pattern (members 8, 13). These differences do not depend on the δ treshold and are robust. The eastern equatorial dynamics in the Pacific determines most of the variance of the *E* signal, so that differences in the *E* shape play a minor role in the network inference.

The distribution of domains in the tropical areas resembles the observed one. Independently of the detrending method, δ-MAPS identifies a strong Indian Ocean domain (*IO*) extending over the western portion of the basin and, in some members, a much weaker domain in the eastern part. This is indicative of a known overestimation of the Indian Ocean Dipole in CESM (Cai & Cowan, 2013). All runs have domains in the horseshoe region that are strongly anticorrelated to *E*, even if their shape and size vary. The identification of the domains in the tropical Atlantic region, on the other hand, depends on the detrending choice for several ensemble members. Whenever the ensemble mean trend, with its band of equatorial warming, is removed, the tropical domains north and south of the equator merge in about 50% of the cases (e.g., members 12 and 22 in Figure 5). Incidentally, if the CESM ensemble trend is removed in HadISST and COBEv2, the merging of the tropical Atlantic domains is recovered in these data sets as well.

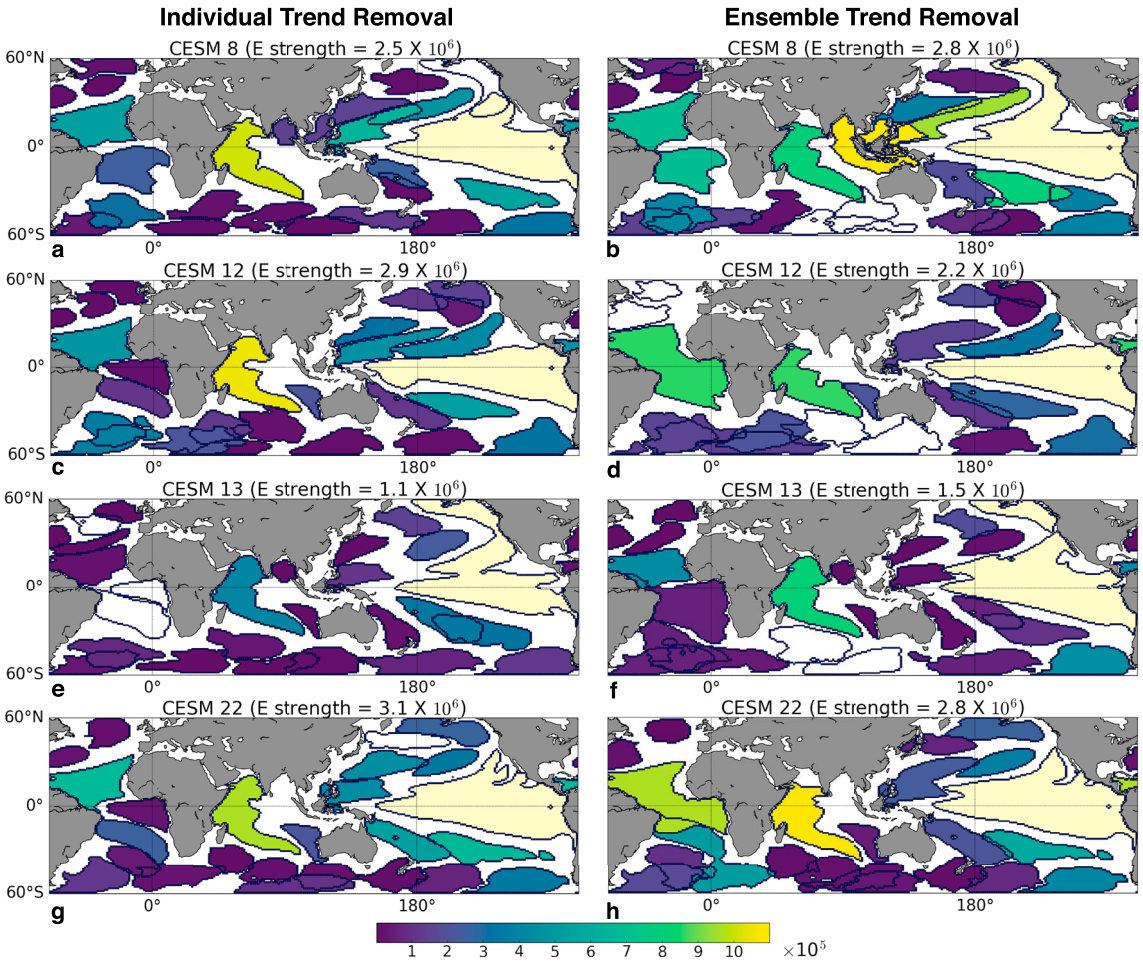

Figure 5. Strength maps for members 8, 12, 13, and 22 after removing the individual trend (left panels a, c, e, g) and the ensemble mean trend (right panels b, d, f, h). CESM = Community Earth System Model.

In Figure 6 the networks inferred between the seven domains corresponding to the strongest in the HadISST and COBEv2 are shown for the same four members as before, with all others in the appendix (see Figure C3). Here TA_S identifies whichever Atlantic domain comprises the equator; if the horseshoe pattern is composed of multiple domains, the strongest ones to the north and south of the equator are chosen as HS_N and HS_S, respectively.

Figure 6 reveals a strong internal variability in the inferred networks whenever individual trends are removed, despite similarities in the correlograms of the signal of most domains in the different members. This indicates that the network differences result from the strength of some modeled connections, which are near the statistical significance level. Overall, in all members correlations from the *E* domain tend to be overestimated (see Figure C3). Previous work (He et al., 2017) suggests that this bias may be caused by an overestimation of the thermodynamic response of the tropics to ENSO in CESM. A more in-depth analysis on this bias is presented in section 7. While shape and size of domains do not depend significantly on the trend removed (individual vs. ensemble) except for the tropical Atlantic region, more positive links are captured by the networks if the ensemble mean trend is subtracted in all members (Figures 6). It is instructive to compare changes for members 8 and 13. The first is characterized by a linear trend similar in pattern and intensity to the observed one; its network is also similar to that of the observational data sets, as quantified in the next section. When the ensemble mean trend is removed, fewer and less intense negative links are identified. The linear trend of member 13, on the other hand, is characterized by a pattern reminiscent of the PDO in its positive phase. When this pattern is subtracted, the Pacific variability is modified and fewer links from the *E* domain are found. By removing the ensemble mean trend, positive correlated links such as the one from *E* to the TA_N and *SP* domains are restored.

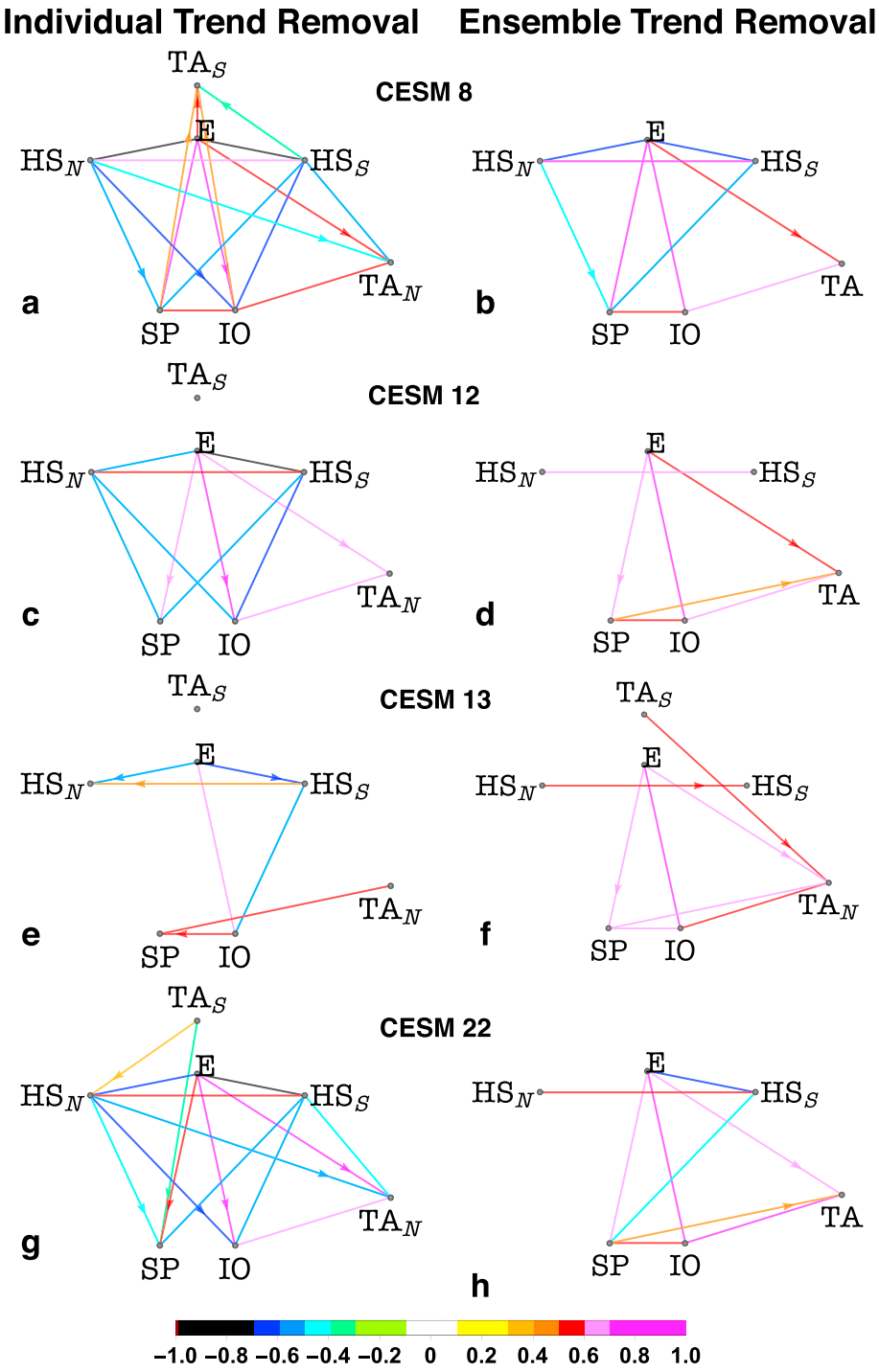

Figure 6. Networks between strong tropical domains for members 8, 12, 13, and 22 after removing the individual trend (left panels) and the ensemble mean trend (right panels). CESM = Community Earth System Model.

Finally, we focus on the link between the TA_S and the E domains in the case of individual trend removal. All members but one display opposite to the observed or no connection between these two domains. Only member 26 has a link with similar sign and lag to HadISST and COBEv2, even if weaker than in the observations. The correlogram between E and TA_S domains reveals a strong internal variability (not shown). While nearly all connections can be regarded as robust within the ensemble, this important link appears fragile.

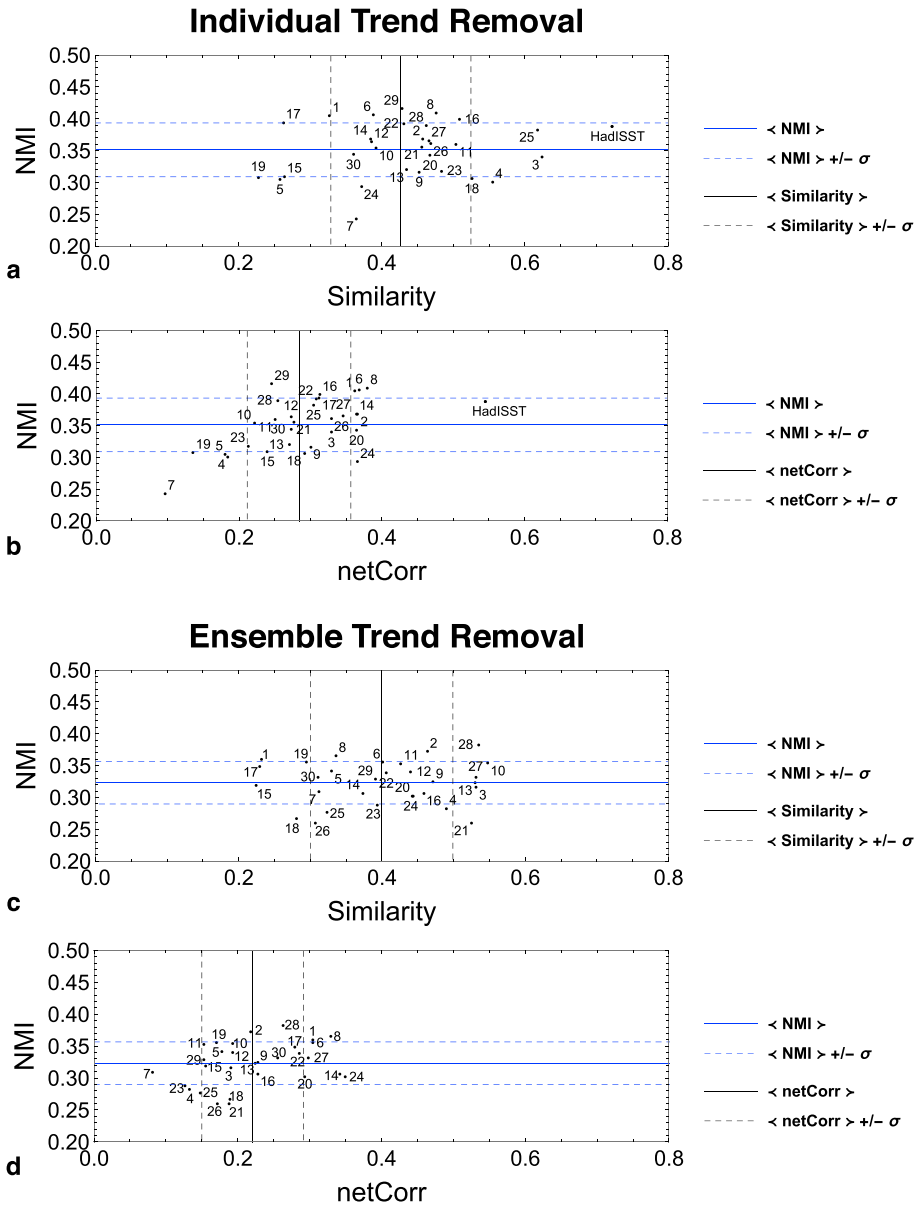

Figure 7. Normalized Mutual Information (NMI) versus S and NMI versus netCorr when removing the individual trend (panel a and b) or the ensemble mean trend (panel c and d), respectively. All networks are compared to COBEv2. The NMI, Similarity, and netCorr metrics compare networks respectively in terms of shapes and sizes of their domains, their strength maps, and network topology. Continuous lines indicate the ensemble mean of the metric of interest, and dashed lines delimit the ensemble standard deviation.

6. Ensemble Evaluation

The metrics introduced earlier are used to quantitatively compare the modeled and observed networks. In Figure 7 the SST networks for all ensemble members, along with that of HadISST, are compared to the network obtained using COBEv2 in the (S, NMI) and (netCorr, NMI) spaces. Differences across members can only be due to the internal variability of the (modeled) climate system. The areas defined by $\sigma_{\mathrm{NMI}} \cdot \sigma_{\mathrm{S}}$ or $\sigma_{\mathrm{NMI}} \cdot \sigma_{\mathrm{netCorr}}$ quantify such variability in CESM.

In the case of individual trend removal, the NMI of the HadISST network is inside the range defined by $\langle \mathrm{NMI}_{\mathrm{CESM}} \rangle + \sigma_{\mathrm{NMI}_{\mathrm{CESM}}}$, indicating that, on average, the CESM model reproduces well the spatial extent and shape of the observed domains. Large differences between the modeled and observed climate arise from the

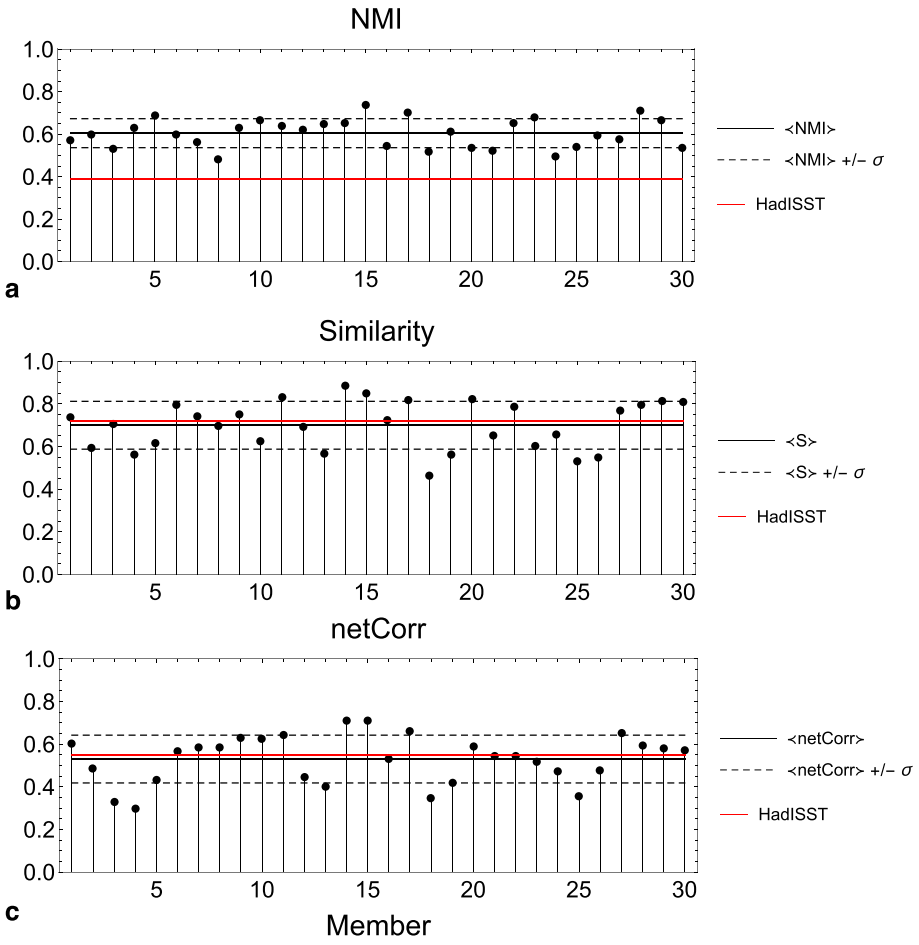

Figure 8. Differences in network properties for each member whenever the individual or ensemble mean trends are removed. NMI (a), S (b), and netCorr (c). Continuous black line indicates the ensemble mean of the metric of interest while dashed black lines delimit the ensemble standard deviation. Continuous red line indicates the values of NMI, S, and netCorr for observational data sets (HadISST vs COBEv2). NMI = Normalized Mutual Information.

connectivity properties of the network. Discrepancies are indeed evident when comparing the networks in terms of domain strengths with the S metric and further increase when using netCorr.

Members 3, 25, 16, 4, 18, and 11 are among the ones with greater S. Being *E* as the dominant domain in the SST network, it is expected that in runs with large S the *E* strength compares well to observations. This is indeed the case as shown in Figure 9. Having similar domains' strengths is a necessary but not sufficient condition for two networks to have comparable structure, and indeed, these members span different values of netCorr, not always close to the ensemble mean ⟨netCorr⟩. It is instructive to look more closely at member 4, which is characterized by a low netCorr but high S. Connections between the strongest domains are not well captured by it (see Figure C3), and the *E* domain has too few links; the relatively large value of *E* strength is achieved through a large STD of the *E* signal itself. There are also members with low S but large netCorr such as 1, 17, and 24. For these members the similarity bias derives from an overestimation of the strengths of the strongest domains. Indeed, the CESM ensemble members that closely capture the observed network structure tend to have domains that are too strong compared to both observational data sets, as further discussed in section 7. The netCorr is therefore a powerful metric when comparing modeled and observed network structures and should always be used to complement the Similarity one.

If the ensemble mean trend is removed, all three metrics deteriorate slightly in the comparison with COBEv2, as to be expected. Differences in NMI originate, for the most part, from the identification of a single

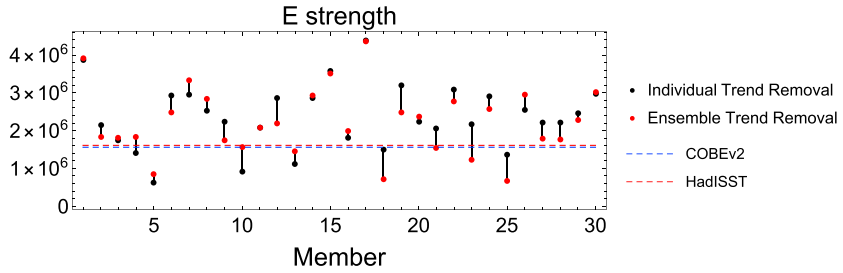

Figure 9. Comparison between the E strength after removing the individual (black) or the ensemble mean trend (red). Dashed blue and red lines indicate the E strength value for COBEv2 and HadISST, respectively.

tropical Atlantic domain. The shape and size of the other domains is generally robust and independent from the detrending choice (see Figures C1 and C2). Again, greater differences are found in the network structures. When removing the ensemble mean trend we obtain, on average, more positive links associated with the warming residual common to several of the strongest domains. As a result, the anticorrelation between E and the HS_N and HS_S domains is statistically significant in fewer members, masked by the residual trend that has the same sign across the whole tropical Pacific (see Figure 6).

The impact of the choice of trend removal on the final network is further investigated through the evaluation of the changes in each metric for all members (Figure 8).

The NMI, when comparing networks for the same member with different detrending strategies, is high ($\langle \text{NMI} \rangle = 0.60$) and the spread across the ensemble is contained ($\sigma_{\text{NMI}} = 0.06$). For reference, the NMI obtained comparing the HadISST and COBEv2 networks was $\text{NMI}_{\text{HadISST}} = 0.39$. The S metric and netCorr have mean values of $\langle \text{S} \rangle = 0.70$ and $\langle \text{netCorr} \rangle = 0.53$, only slightly lower than those found comparing HadISST and COBEv2 ($\text{S}_{\text{HadISST}} = 0.72$ and $\text{netCorr}_{\text{HadISST}} = 0.55$), but the spread across the ensemble is more substantial than for the NMI metric ($\sigma_{\text{S}} = \sigma_{\text{netCorr}} = 0.11$). The topology of (CESM) SST networks is then, on average, independent of the trend removal method. However, relatively large σ_{S} and σ_{netCorr} are indicative of the removal of some internal variability at the level of single-ensemble members. Therefore, in some cases removing the individual trend on a time scale of 35 years can coincide with the removal of a portion of the climate variability signal. For example, in ensemble member 13 differences are evident: its linear trend (Figure 4) is reminiscent of a strong positive ENSO/PDO pattern, and its removal impacts the network connectivity in the Pacific. Given the heterogeneity in trends though, a cause-effect relation of the individual versus ensemble mean trend removal common to all members cannot be identified. The strongest difference in netCorr is found for member 4; for this run the removal of the ensemble mean trend results in a network with a strong tropical Atlantic domain (Figure C2) in correspondence of an intense residual warming confined in the equatorial Atlantic.

Finally, we quantify how the strengths of the strongest domain, E, vary depending on the detrending choice (Figure 9). For most members, the E strength is nearly independent of it. It is worth noting, however, that whenever the individual trend has a pattern similar to the observed one (for example, in the case of members 8, 10-same sign, and 13-opposite sign), then the strength the E domain increases slightly when the ensemble mean trend is removed.

7. Biases in the Modeled Network Properties

In this section we investigate biases in the SST network structure of the CESM ensemble when compared to that of observational data sets. Biases are robust—across members—differences the model and the observations, as opposed to differences that may be linked to the model internal variability. We verified that results are, on average, independent of the detrending method and discuss only the case of individual trend removal, which is consistent with the detrending applied to the observational data sets. We focus on connections and statistical properties of the E, TA_N, and IO domains, but the analysis holds for all tropical domains.

7.1. Overestimation of the Thermodynamic Feedback to El Niño Events

Positive correlations between E and tropical domains are always overestimated in CESM (see Figure C3). This bias stems from an overly strong thermodynamic response of the tropics to El Niño episodes (Chiang & Sobel, 2002; Chiang & Lintner, 2005; Saravanan & Chang, 1999) and is common to all ensemble members. As

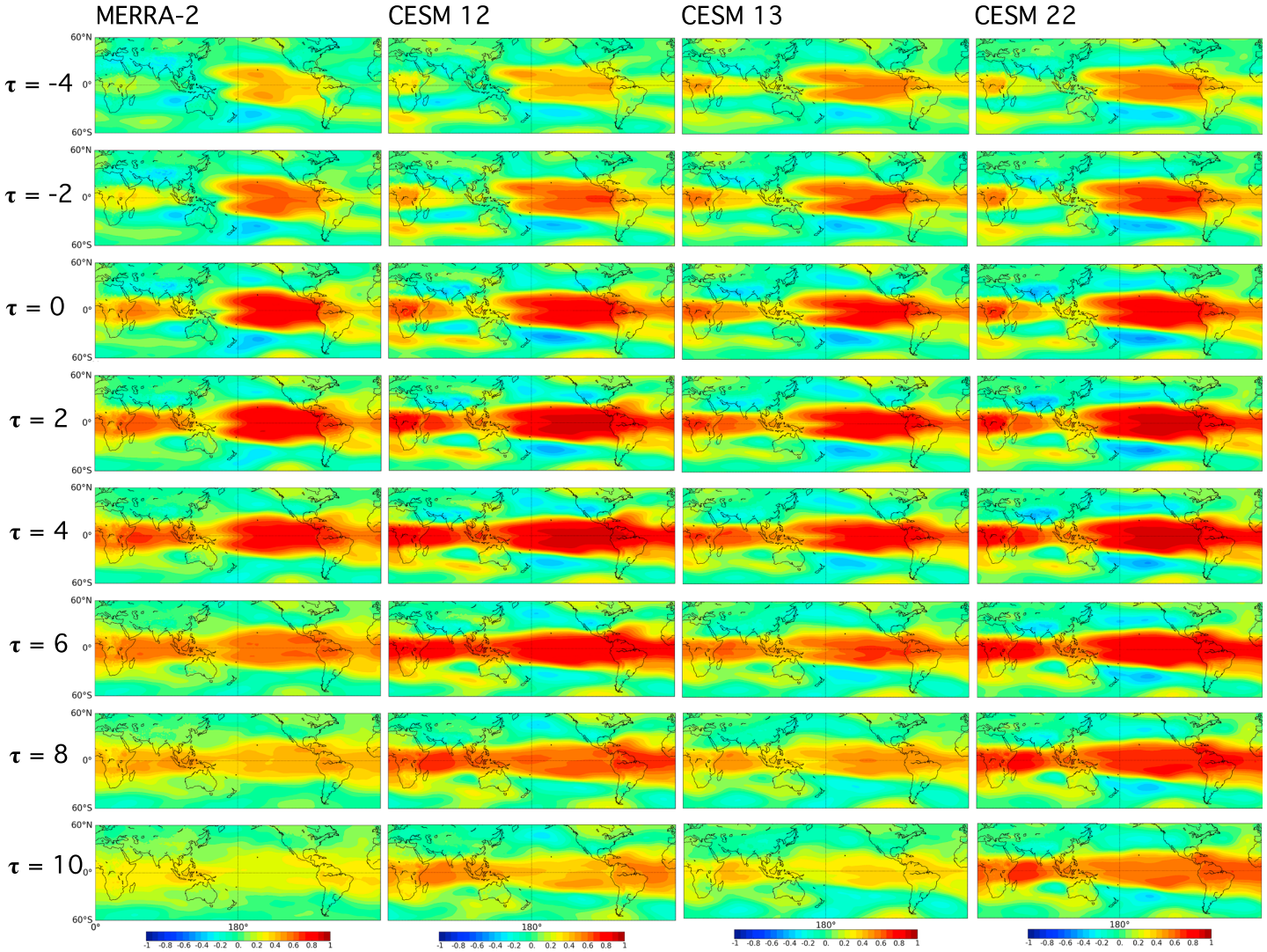

Figure 10. Maps of lag correlation coefficients between the *E* signal (as computed by the sea surface temperature networks) and the air temperature-detrended anomalies integrated from 900 to 200 mbar (tropospheric temperature anomalies). Each column refer to the reanalysis (MERRA-2) or ensemble member (12, 13, and 22). Each row indicates the lag τ in months. For instance, $\tau = 2$ indicates a 2-month leading of the *E* signal on tropospheric temperature anomalies. CESM = Community Earth System Model.

discussed also in Bracco et al. (2018), tropical SST variability is linked to that of the eastern Pacific through a thermodynamic response following El Niño events. During an El Niño episode, the heat transferred from the ocean to the atmosphere in the tropical eastern Pacific is transported to the east by Kelvin waves and to the west by Rossby waves (Gill, 1980; Matsuno, 1966). This Gill-Matsuno-type response to SST warm anomalies in the *E* domain induces a more stable atmospheric column in the tropical troposphere, inhibiting convection and causing mixed-layer warming in tropical oceans away from the equatorial eastern Pacific. This is captured by the SST networks in terms of positive weight links between the *E* domain and the TA_N and *IO* domains.

This equatorial heat-induced wave response is quantified in Figure 10. Here we computed the lag correlations between the *E* signal and monthly air temperature-detrended anomalies integrated from 900 to 200 mbar for the reanalysis data sets (SSTs from COBEv2, but identical results are obtained for HadISST, and air temperature fields from MERRA-2) and three ensemble members (12, 13, and 22). Members 12 and 22 are among those with the strongest leadings of the *E* domain on tropical domains in the SST networks (see Figure C3). Member 13 instead has relatively (to CESM) weak link weights associated with the *E* domain.

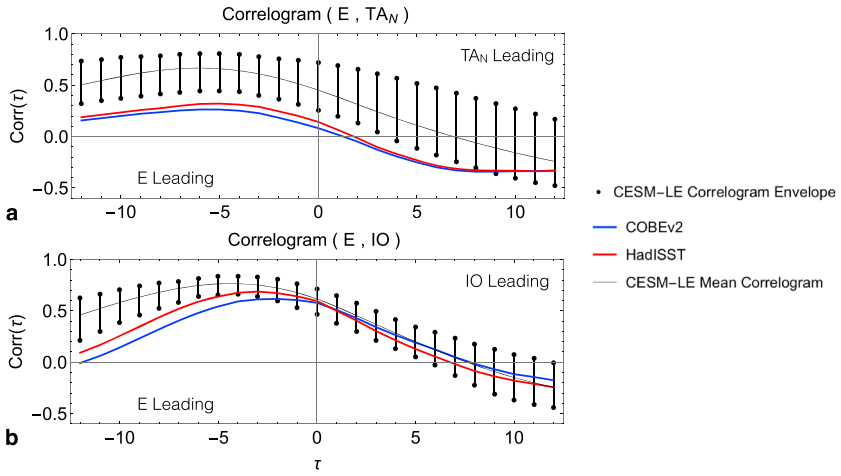

Figure 11. Correlograms between the E and (a) the TA_N and (b) the IO signals in HadISST, COBEv2, and 30 members of the CESM. The CESM envelope includes results from all ensemble members. The solid line indicates the ensemble mean. Correlograms are computed from −12 to 12 months. CESM-LE = Community Earth System Model Large Ensemble.

Following Chiang and Sobel (2002), the response can be split in three different phases: a growing phase (from $\tau \sim -4$ to $\tau \sim 0$ months), a mature phase (from $\tau \sim 0$ to $\tau \sim 4$ months), and a decaying phase (from $\tau \sim 4$ to $\tau \sim 10$ months). The growing phase corresponds to a large heat transfer to the troposphere during the development of an El Niño and the resulting generation of equatorial wave fronts transporting the eastern Pacific anomalous heating to other tropical areas. The mature phase corresponds to an increase in magnitude of the correlation between the E signal and the tropospheric temperature in the tropical band and is associated to a uniform heating of the tropical regions impacted by El Niño. Finally, in the decay phase we see a gradual loss in correlations between the E signal and the tropics.

All three members differ from the reanalysis in the growing phase: even if the correlation pattern is reminiscent of the observed "dumbbell shape" (Chiang & Sobel, 2002) in the eastern Pacific, stronger than observed values are present in the tropical Atlantic and central Africa at $\tau = -2$. This suggests a faster than observed propagation of the eastern Pacific signal by wave dynamics in CESM. During the mature phase the correlations are overestimated and more uniformly distributed across the tropical belt in members 12 and 22, while member 13 is closer to MERRA-2 in the response magnitude but nonetheless overestimates the signal over the Indian Ocean, Atlantic Ocean and Africa. Finally, an important difference is found in the decay phase that is too long in the model. Specifically, even after lags as large as $\tau = 10$ months strong correlations remain in the equatorial band, and this holds also for member 13, notwithstanding the lower intensity.

The overestimation of this specific dynamical teleconnection can be quantified by the correlograms between E, TA_N, and IO domains in all model members and reanalyses, as shown in Figure 11. The E lead into other tropical domains depends indeed strongly on the strength of the thermodynamic link. Values significantly higher than in the reanalyses are found in CESM for the E connection with the TA_N domain. Positive links from E to the IO are generally closer to those in the observations for the lag range $\tau = [-3, 0]$ but are overestimated for $\tau < -3$ months.

7.2. Overestimation of Tropical Domains Strengths

Consistently with the overestimation of the thermodynamic link, the strengths of the tropical domains are too strong in CESM compared to the HadISST and COBEv2, as shown in Figure 9 and in Figure 12 for the E, TA_N, and IO domains. In the case of the TA_N and IO domains, this is not due to an overestimation of the STDs of their own signals (Figures 13b and 13c), but to the overestimation of the STDs of the modeled E. Additionally, the relative strengths of E, TA_N, and IO covary across members. Indeed, the correlation coefficient between the strengths of the E and IO domains for members 1 to 30 is $c.c. = 0.79$, and those of E and TA_N is $c.c. = 0.83$. Taken together with the robust leading of the E domain, this implies that the strength of the TA_N and IO domains is controlled by the links with the eastern Pacific.

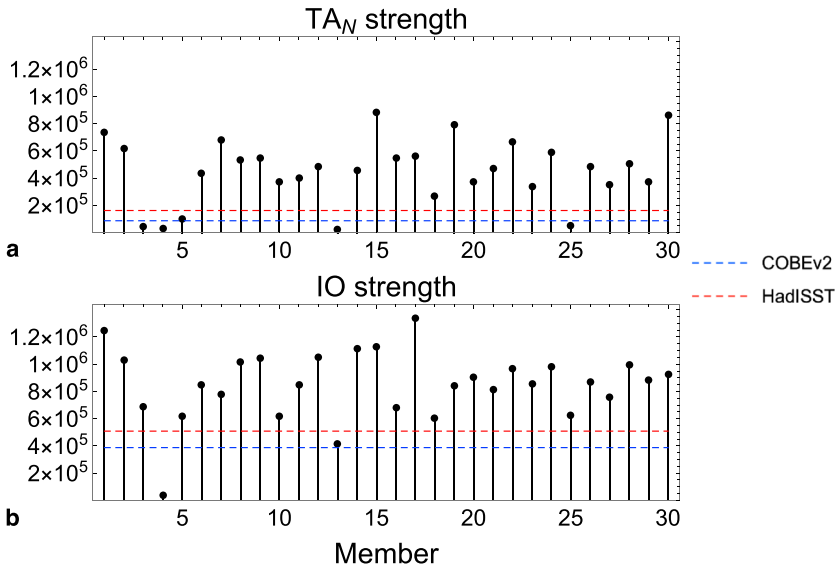

Figure 12. Strength of the (a) TA_N and (b) *IO* domains for 30 CESM members, HadISST, and COBEv2. CESM = Community Earth System Model.

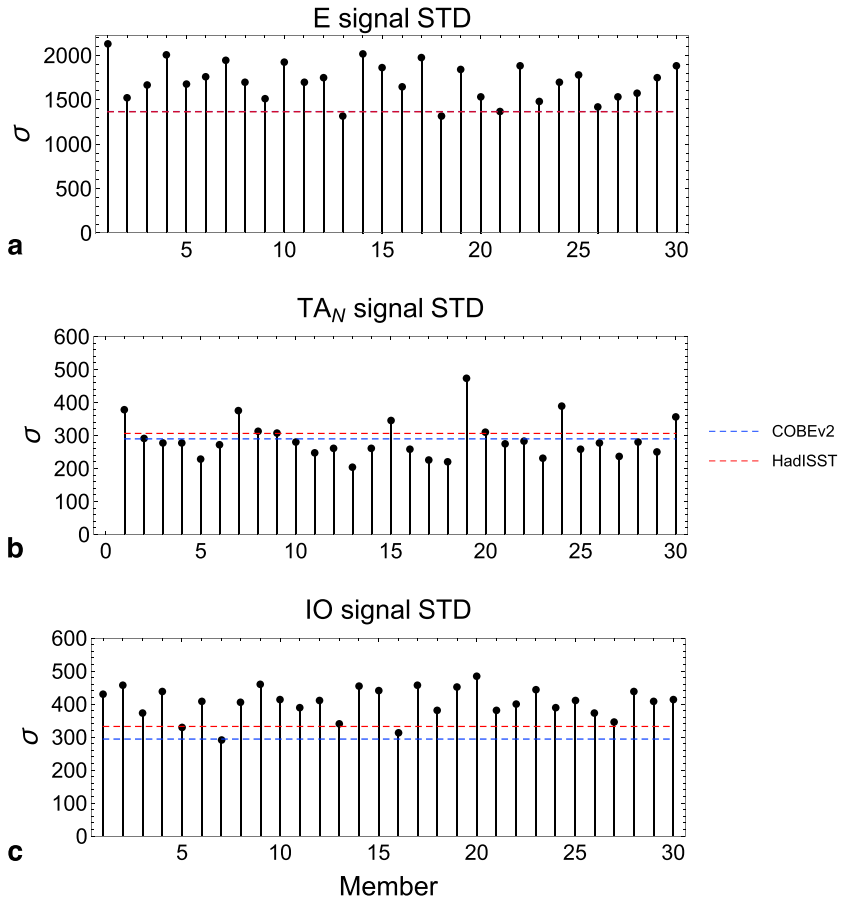

Figure 13. Standard deviations of the (a) *E*, (b) TA_N, and (c) *IO* signals for 30 CESM members, HadISST, and COBEv2. CESM = Community Earth System Model. STD = standard deviation.

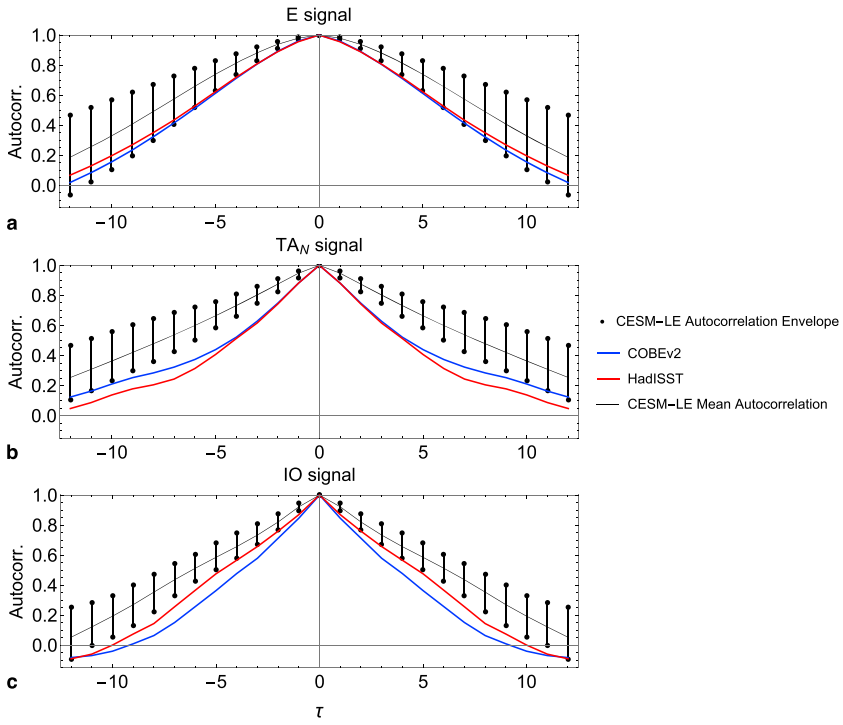

Figure 14. Autocorrelations of the (a) E, (b) TA_N, and (c) IO signals for 30 members of CESM-LE, HadISST, and COBEv2. The correlogram envelope embeds all values found in the ensemble. The solid line indicates the ensemble mean. Autocorrelations are computed for the lag range $\tau \in [-12, 12]$ months. CESM-LE = Community Earth System Model Large Ensemble.

7.3. Overestimation of Domains Signals Autocorrelations

Lastly, the autocorrelations of the E, TA_N, and IO signals across all model members are biased toward very large values, as shown in Figure 14 where autocorrelations are computed for a lag range $\tau \in [-12, 12]$ months. Values are as high as ~0.6 for lags as long as 10 months (see Figure 14a). Only five members (2, 9, 12, 18, and 21) have the autocorrelation of the E signal that compares well with the observations. For these members, the power spectrum of the E signals is also similar to the observed ones. In all other members the ENSO episodes repeat with a well-defined periodicity, resulting in strong autocorrelations.

The overestimation of the autocorrelations impacts the inferred networks. For example, the networks for members 5 and 10, both with very high autocorrelations, have few statistical significant links once the autocorrelations are accounted. These results are largely independent on the detrending strategy. For completeness, correlograms between E, TA_N, and IO domains along with their autocorrelations, for the case of ensemble mean trend removal are shown in the appendix in Figures E1 and F1.

8. Climate Networks in Time

In recent years, a few number of studies investigated the temporal evolution of climate networks. The focus of these works ranges from the temporal variability of surface air temperature networks (Radebach et al., 2013) to new methods to characterize the evolution of climate networks (Tupikina et al., 2014), to the study of their temporal stability (Berezin et al., 2012). The majority of these contributions focus on reanalyses data.

Here, we evaluate the evolution in time of the SST climate networks in the observational data sets and in a subset of 10 members of the CESM ensemble. We focus on the evolution of single-network properties (i.e., domains strengths) and in changes in time of specific connections. We then attribute differences between observations and models either to model biases or internal variability.

Networks are inferred over periods of 51 years and computed with a sliding window of 2 years for observational data sets from 1920 to 2015, and 3 years for the ensemble members from 1920 to 2100. All data sets are analyzed at the lower resolution of 2.0° × 2.5°, and in each period the SST data are detrended. We have shown in section 7 that network changes in the most recent period are, on average, not strongly affected by

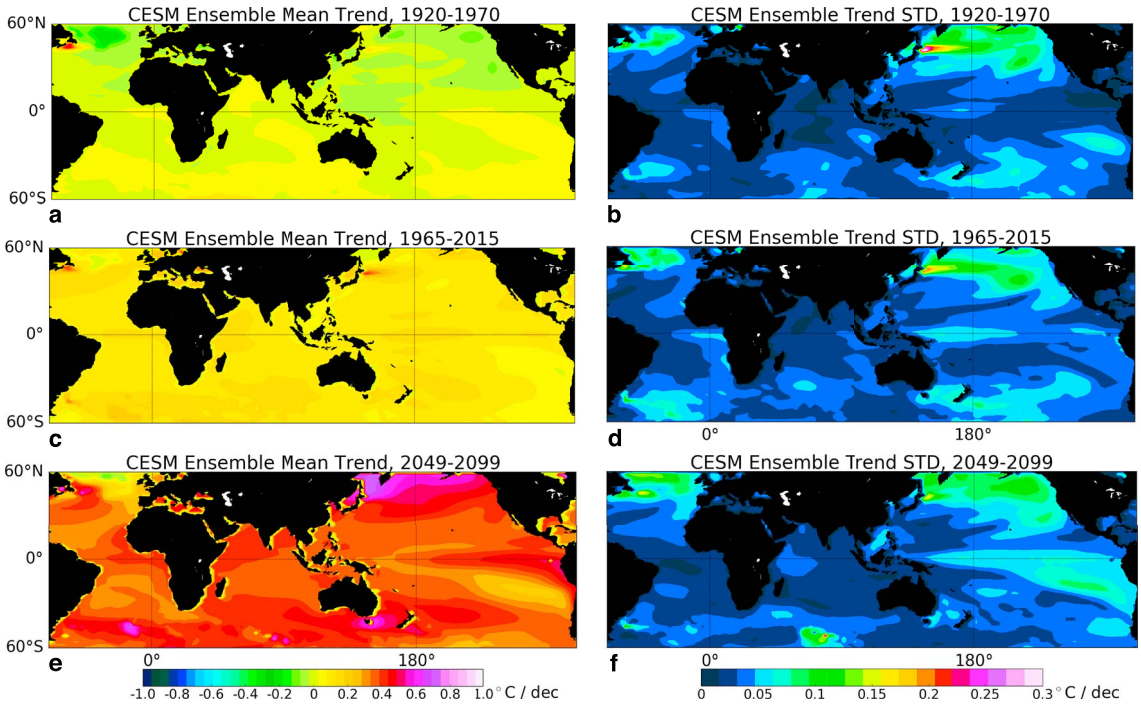

Figure 15. Ensemble mean trend and trend standard deviation for periods 1920–1970 (a,b), 1965–2015 (c,d), and 2049–2099 (e,f). CESM = Community Earth System Model; STD = standard deviation.

the detrending choice (i.e., whether the ensemble mean or single-member trend is removed). Differences quantified in Figure 8 between networks with individual member or ensemble trend removed are on average analogous to those between the HadISST and the COBEv2. Furthermore, we verified that, for periods of 51 years, the pattern of the ensemble mean trend and its STD do not change much over time (Figure 15). The mean trends are characterized by an overall global SST warming, as to be expected given the evolution in radiative forcing, which is more uniform than what was obtained when considering the most recent 35 years. The STD of the ensemble trend is also similar across periods and smaller than during 1980–2015. The variability is generally stronger in the North Pacific and North Atlantic regions and smaller elsewhere. Noticeably, there is an increase in STD in the equatorial Pacific over time. This result is in agreement with the analysis performed by Liguori and Di Lorenzo (2018) on the same model ensemble, and suggests a possible increase in strength in the coupling between tropical and extratropical decadal variability in the Pacific in response to a more energetic North Pacific Meridional Mode; the Pacific tropical variance, however, remains contained. We consider it therefore reasonable to analyze network changes over time only in the case of individual trend removal.

The size and shape of domains are found to be largely independent of the period analyzed in all data sets considered (see Figure 17 later in this section). The networks, however, vary in their mean strengths, mainly in response to changes in the amplitude and variance of the E signal. This is quantified considering the time evolution of the STD of the E signal for each period and of the tropical mean strength (TMS), computed as the weighted averaged strength of all domains over the latitudinal range [30°S, 30°N] (Figure 16).

In both HadISST and COBEv2 there is a linear positive trend in E signal STD, but significant only for HadISST according to a Student's t test with 95% confidence level. Differences between the two observational data sets are larger in periods before 1940–1990 and smaller thereafter. From 1920–1970 to 1971–2021 the CESM ensemble mean E STD have a positive trend similar to that of HadISST, but the E signals are generally overestimated. In this time span, the trend is statistically significant, again according to a t test, in seven members along with the ensemble mean. After the 1971–2021 period, eight out of the 10 members have no significant trend, and the STD of the E signal continues to grow steadily only in two runs (members 3 and 5).

Recently, Zheng et al. (2018) investigated changes in ENSO amplitude in the CESM-LE and the role of internal variability by computing the 50-year running STDs of the Niño 3 index. They found a strong internal

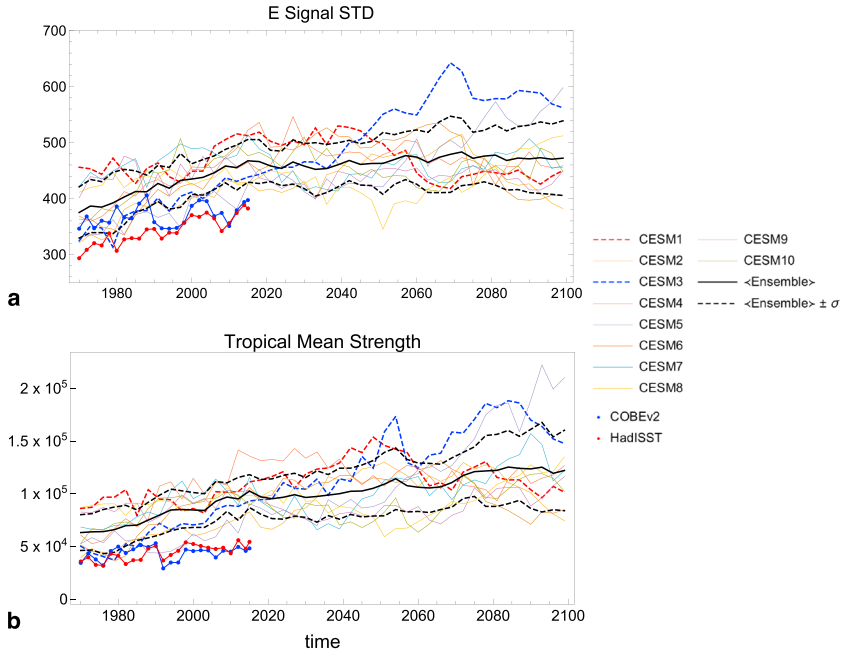

Figure 16. Time evolution of tropical mean strength for 10 members of the CESM-LE, HadISST, and COBEv2. The years on the *x* axis denote the last in the 51-year periods analyzed. CESM-LE = Community Earth System Model Large Ensemble

variability in the amplitude of the ENSO signal and argue that a minimum of 15 ensemble members should be considered to decouple the role of internal variability and forced response to ENSO changes. Differing from their study, here we consider SST anomalies over a larger region, specifically the *E* domain identified by δ-MAPS, and the STD spread is contained. We verified that 10 members are sufficient to characterize the projected evolution of the *E* amplitude by removing one or two members chosen randomly from the 10 considered.

Focusing on the TMS evolution, a small but significant trend is found in the HadISST data set, in which the correlation between the time series of the STD of the *E* signal and the TMS is 0.80. In COBEv2 no significant trend is present and the correlation drops to 0.63. In CESM eight of the members analyzed, along with the ensemble mean, have a statistical significant trend over the 1920–1971 to 1971–2021 period, and the TMS trend is much stronger than in the HadISST or COBEv2 by the end of the historical integrations in all members. Afterward, the positive trend remains significant in five members, along with the ensemble mean.

The overestimation in the amplitude of the *E* signal STD in CESM, due to the overestimated thermodynamic response of the tropics to the *E* variability (see section 7), translates in an even larger overestimation of the TMS, which evolves, amplified by the other tropical domains, following the *E* signal. For the members analyzed the average correlation between the *E* STD and TMS is 0.78 with a STD of 0.20.

As previously discussed, changes in tropical mean strength are not related to changes in shapes and sizes of the domains, but rather to changes in their connectivity. Figures 17a–17d show the *E* link maps for the first and last 51-year-long periods in HadISST and COBEv2. There is no qualitative change in the overall structure of domains and links to/from the *E* domain, except for those between the *E* and South Tropical Atlantic domains that lack in robustness. In the HadISST case there is a moderate increase in the link weight with the domains in the horseshoe region, particularly in the Southern Hemisphere, and with the Indian Ocean moving from the first to the last periods. Link maps are shown also for CESM members 1 and 3. In member 1 the STD of the *E* signal and the TMS follow broadly the evolution of the ensemble mean. There is a general strengthening between the first and second periods considered, and then link weights remain stable. Member 3, on the other hand, is one of the two for which the *E* signal STD continues to grow in the future, with a peak in the projections for 2019–2069, shown in the figure. Links, both positive and negative, strengthen during the whole integration.

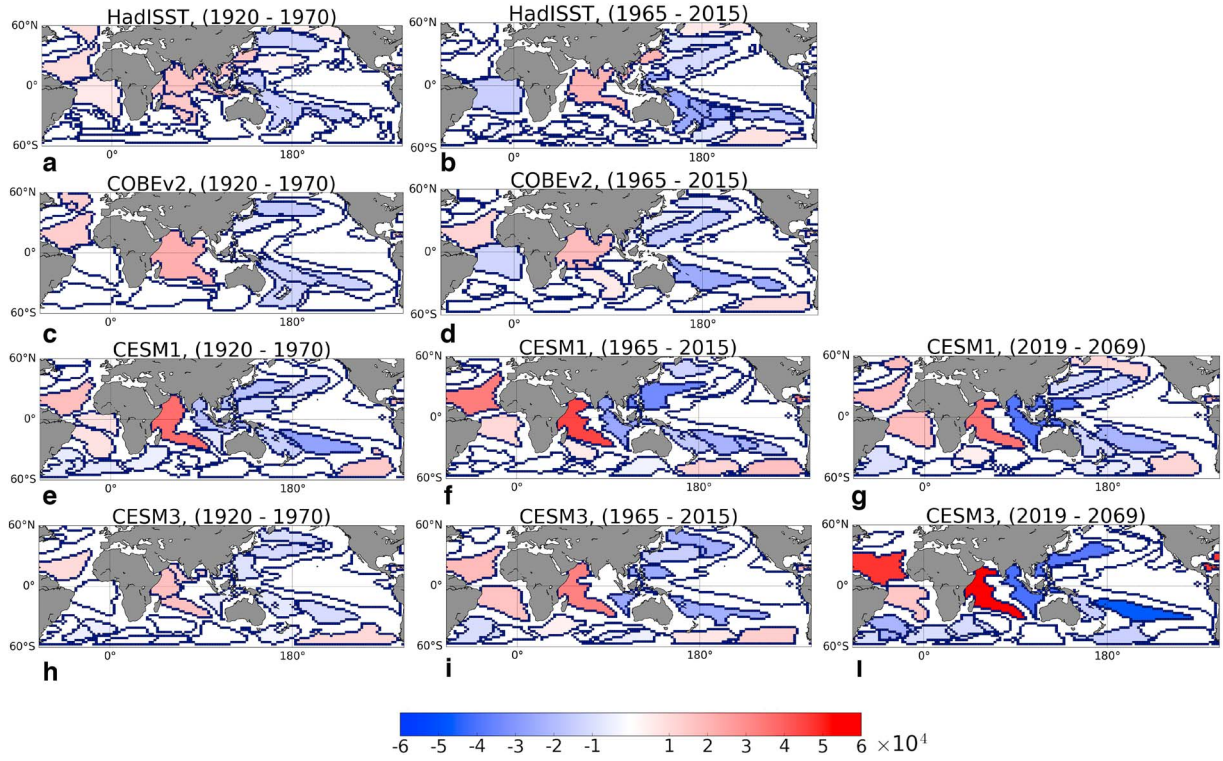

Figure 17. *E* domain link maps. The color of each domain quantifies the weight of its connection with the *E* domain. CESM = Community Earth System Model.

The changes in connectivities from the *E* domain over time are further visualized by showing the correlograms of the *E* domain from/to the *IO*, TA_N, and TA_S domains. In the case of the observations (Figure 18), for which the correlograms are similar across the data sets, the leading of *E* to the *IO* domain is the most robust link, with the *E* domain always leading the Indian Ocean one (see Figures 18a and 18b). Leading positive, but weaker, correlations are also found between the *E* and TA_N, with the *E* lead being stronger between the periods 1926–1976 and 1950–2000, and weaker thereafter (Figures 18c and 18d). Interestingly, Figures 18e and 18f show that in the observations the lead of the South Tropical Atlantic on the eastern Pacific is time dependent and active only in certain decades, in agreement with the analysis by Martín-Rey et al. (2014).

The correlograms for two CESM members, numbers 1 and 3 are shown in Figure 19. Due to the thermodynamic bias, the leadings of *E* on the *IO*, TA_N, and TA_S domains are robust, especially for the first two links, and always overestimated. In the case of member 3 correlations with *IO* and TA_N grow during most of the 21st century. The relation between *E* and TA_S, on the other hand, displays greater variability in time, and a lead of the TA_S domain on *E* is apparent during some decades especially in member 1. In the historical period 1980–2015 we found that only one member (number 26) captured the leading of TA_S on *E*, while all others showed no link or an *E* lead. This last analysis suggests that the dynamic teleconnection between the TA_S and *E* domains is captured, at least partially, by CESM, notwithstanding the masking caused by the overestimated thermodynamic teleconnections from *E* onto all tropical domains, but is highly variabile in time. Therefore, the lack of this specific link in most members cannot be attributed to a specific bias. A more detailed investigation of this last point along with the analysis in time of all 30 ensemble members (as suggested by Maher et al., 2018) is left for future studies.

9. Summary

A new framework to analyze and compare climate fields is presented and applied toward the investigation of SST fields in observational data sets and climate models outputs. The framework is built upon δ-MAPS (Fountalis et al., 2018), a network methodology that aims at identifying the spatially contiguous components of a system that contribute in an essential way to its dynamics. δ-MAPS then infers the connections between those components or domains, and in doing so it accounts for autocorrelations (Guez et al., 2014). Compared to previous work (Fountalis et al., 2014), major improvements of δ-MAPS, besides the care taken to

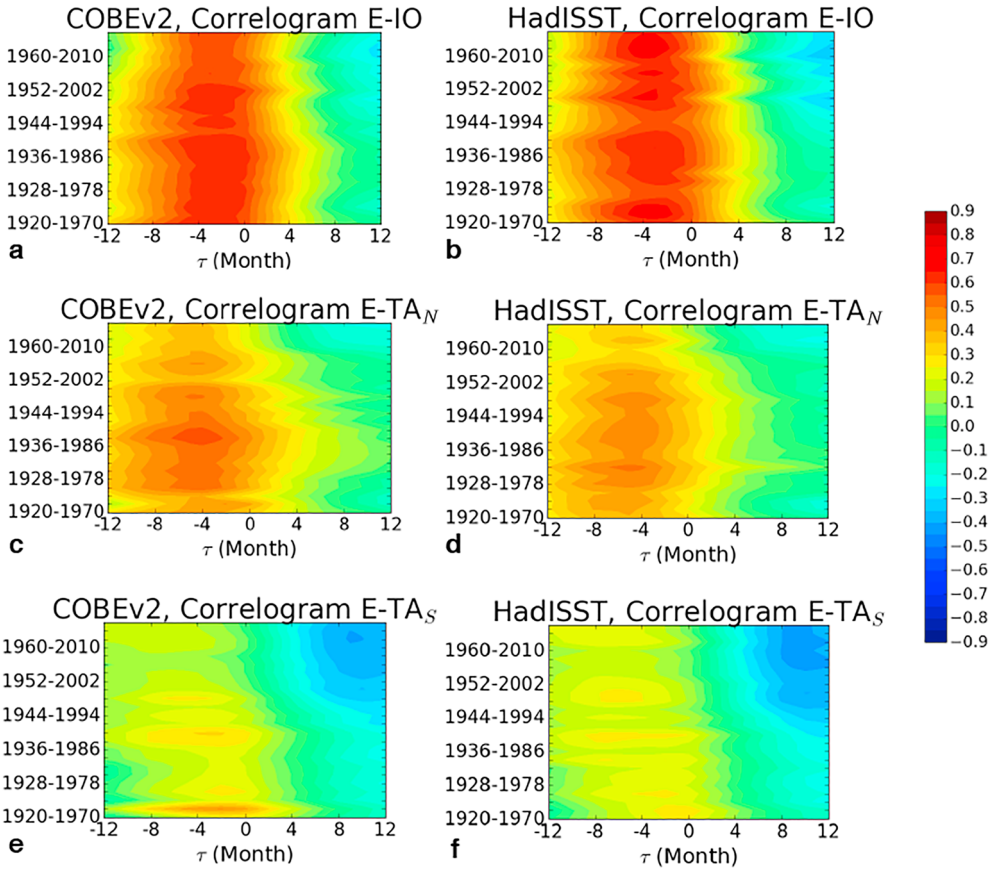

Figure 18. Correlograms in time between *E* and *IO* (a, b), TA_N (c, d), and TA_S (e, f) signals in HadISST and COBEv2. Correlograms are computed from −12 to 12 months (*x* axis) and from period 1920–1970 to 1965–2015 (*y* axis). The colors quantify the cross correlations between signals.

account for autocorrelations, include domains overlapping, the possibility of capturing lagged relationships, and the identification of grid cells that do not belong to any domain. We emphasize that this framework does not provide informations on dynamics and/or causality. However, topological differences between observed and modeled networks can be used to uncover and track model biases due to the poor representation of dynamical processes. A set of four metrics complements the data mining package and allows for characterizing the domains properties and their connectivity patterns. These metrics are adopted from the literature or developed with the goal of allowing the comparison of domains and their connections in climate studies (see section 2.2). Differences in domains shape and size are quantified using the NMI, the distance in domains strength between two networks is quantified by the Similarity metric, and the time evolution of each domain is characterized by its strength. Furthermore, the newly developed netCorr allows to quantify differences in network structures, accounting for temporal ordering and domains overlapping.

A major objective of δ-MAPS is to infer linkages across domains in the same climate field and eventually across different components of the climate system through analysis of multiple fields and linkages across networks. It represents a scalable framework to quantify differences across data sets and evaluate the impact of perturbations in forcing agents on the topological properties of climate fields. Here we have focused on one of these applications; additional examples can be found in Bracco et al. (2018). We tested the robustness of δ-MAPS on two observational data sets, HadISST and COBEv2, focusing on the period 1980–2015. As to be expected, the strongest domain identified, the *E* domain, corresponds to the ENSO mode of variability and has a signal extremely well correlated with the first principal component of the global SST field. Known teleconnections, such as the positive correlation of the *E* domain with the Indian Ocean and negative correlations with the Pacific horseshoe pattern (Alexander, 2002) are captured, and their relative strength easily quantified. The important lagged leading of the South Tropical Atlantic on *E* that has characterized the last few decades (Rodriguez-Fonseca et al., 2009) is also captured as a key component of the network.

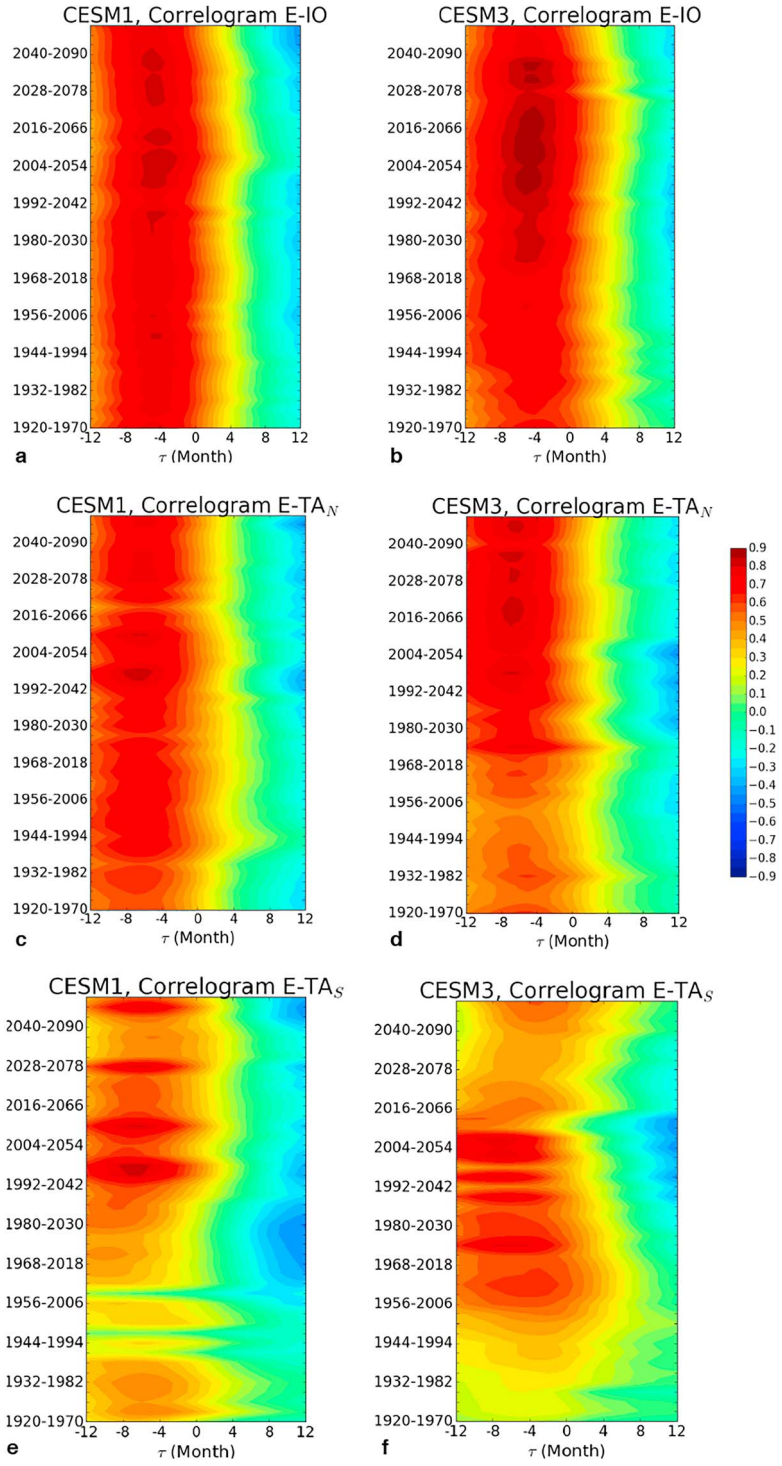

Figure 19. Correlograms in time between the *E* and the *IO* (a, b), the TA_N (c, d), and the TA_S (e, f) signals in members 1 and 3. Correlograms are computed from −12 to 12 months (*x* axis) and from period 1920–1970 to 2049–2099 (*y* axis). The colors quantify the cross correlations between signals. CESM = Community Earth System Model.

To exemplify how the proposed framework can be used to quantify differences across data sets, we compared the network structure of the observational data sets and that of 30 members of the CESM-LE . Networks for the CESM integrations were constructed removing the individual or the ensemble mean trend. The detrending choice does not significantly affect shapes and sizes of the identified domains, as quantified by the NMI metric. For the majority of the ensemble members, the choice of detrending has a negligible impact on the inferred networks: average differences, quantified by the average Similarity ($\langle S \rangle$) and netCorr ($\langle \text{netCorr} \rangle$) metrics, are found to be as large as between the two observational data sets considered. Differences in the networks as function of the detrending choice arise mostly in the tropical Pacific, where negative links such as those between the E and HS_N, HS_S may weaken if the ensemble trend is removed, due to the warming trend in both the E and horseshoe regions.

Independently of the trend removed, the domains identified in the CESM-LE for the period 1980–2015 are similar to those found in HadISST and COBEv2. The connectivity properties, however, differ between the model and observational data sets, as quantified by the Similarity and netCorr metrics. By interpreting the differences in these two metrics, we identified: (i) an overestimation of the STD of the E domain signal, (ii) an overestimation of the thermodynamic response of the tropics to E variability, and (iii) very large autocorrelations of the strongest domains signals. The first and second biases imply stronger than observed correlations from the E domain to the other domains identified in the tropics, greater link weights for domains in this region, and stronger than observed tropical strengths. At the same time, an ENSO signal that is temporally "too periodic" implies greater autocorrelations and lower than observed statistical significance for some connections in about half of the simulations. It is worth noting that a network may have the "right" topology, despite overestimating all domains strengths. This would result in small Similarity but high netCorr values. For this reason, when comparing networks from different data sets, the Similarity and netCorr metrics should be used jointly.

Finally, we investigated changes in network properties over time in 10 members of the CESM-LE, from 1920 to 2100, and observational data sets, from 1920 to 2015, to highlight another possible application of δ-MAPS. In HadISST and in seven ensemble members, the STD of the E domain signal increases over time with a statistically significant trend that, in most runs, lasts until 2020. Only two integrations continue to have a growing STD trend through the 21st century. An increase of the STD of the E signal broadly corresponds to a statistically significant increase in tropical mean strength, or, in other words, to an increase in connectivity among domains across the tropics. We conclude that while the influence and amplitude of ENSO increased in the last century, according to one observational data set and most model runs, CESM projects a weakening of such trend after 2020, despite the continuous increase in greenhouse gas forcing in the scenario considered.

Focusing on the representation of the three major tropical connections, we found that in observations the most stable over time is the lead of E on the IO. The E lead on the TA_N is also robust but weaker. CESM captures both, but overestimates the correlations without differentiating in their amplitude. The observed leading by the South Tropical Atlantic on the E domain is time dependent (Martín-Rey et al., 2014) and absent in the observations before the period 1944–1994. CESM members overestimate the positive, thermodynamically driven link from the E domain into the TA_S one, but capture, during certain decades and in few runs, the dynamic link from the TA_S to E. δ-MAPS would provide a useful tool to investigate more in depth the variability and origin of this connection.

In conclusion, the domain identification algorithm of δ-MAPS enables to reduce the complexity of large climate data sets in an automated way, with several advantages when compared to more traditional dimensionality reduction methods (Fountalis et al., 2018 provides a detailed comparison).

The novelty and utility of the proposed framework consists in allowing for comparing and ranking climate model ensembles in a common, compact, reduced metric spaces (e.g., (NMI, S) and (NMI,netCorr)). This ultimately leads to a simultaneous quantification of model differences in their average error, variability, and representation of teleconnections (origin, strength, relative importance, and time evolution). This information can then be translated into simple visualizations of tradeoffs and mismatches between models, at both global and regional scales, in terms of the spatial distribution and shape of domains and of the topological role of each domain in the network. Moreover, this methodology can be used to compare the same climate model integrated using different parameters, parameterizations or forcing fields, to establish linkages between perturbations to the modeled climate system and its response.

Currently, δ-MAPS uses a simple correlation metric among grid cells to define domains and their linkages. In the future we envision generalizing it to include the analysis of nonlinear phenomena and causal relationships adopting metrics such as the mutual information (Lancichinetti et al., 2009; McDaid et al., 2013) and Granger causality (Granger, 1969).

Appendix A: Heuristics for the K Parameter and δ Threshold

In this appendix we discuss the heuristic for selecting the K parameter and the δ threshold.

A.1. The K Parameter

One of the underlying concepts in δ-MAPS is that the identified domains have epicenter(s) of activity. To identify such epicenters, a local homogeneity field is computed based on the K-neighborhood of each grid cell. The K-neighborhood of a grid cell i, $\Gamma_K(i)$ includes the grid cell and its K nearest neighbors. The local homogeneity of grid cell i is simply the average Pearson correlation between grid cells in $\Gamma_K(i)$ or $\hat{r}_K(i) = \frac{\sum_{m \neq n, \in \Gamma_K(i)} r_{m,n}}{K \quad (K+1)}$. If the local homogeneity of a grid cell is larger than δ and a local maximum in the local homogeneity field, then the grid cell and its local neighborhood are a seed for a domain. Thus, K is a lower bound to the size of a domain. If K is too small, then the local homogeneity field will be noisy (too many epicenters might be identified for a single domain). If K is too large the local homogeneity field will be too smooth and candidate domain epicenters may go undetected. To select an optimal K value, we propose the following: first, we construct domains for a range of K values; then we use the NMI metric (see section 2.2) to construct a pairwise similarity matrix (Figure A1 shown for the COBEv2 data set); finally, we select a K for which (a) the NMI is large and (b) the NMI is large for neighboring values of K to ensure that our results are not sensitive to fluctuations around the proposed K. With the proposed heuristic we set $K = 16$ for COBEv2 and members of the CESM-LE and $K = 22$ for HadISST. For the lower-resolutions data sets used in section 8, the optimal K is 4, which is the smallest K that considers neighbors in all directions.

A.2. Heuristic for δ

The threshold δ defines the minimum degree of homogeneity required to form a domain. It represents the minimum required average pairwise Pearson correlation between the grid cells of a domain; the higher the threshold, the higher the required homogeneity, and therefore the smaller the size of a domain.

The parameter δ is selected as follows. For each pair of grid cells i,j in the data set under investigation, we compute the Pearson correlation at zero lag $r_{i,j}$ and we assess the significance of each correlation using the Bartlett's formula (Box et al., 2011). Under the assumptions that the time series of i and j are stationary with independent and normally distributed errors and of no coupling, $r_{i,j}$ has zero mean and its variance can be

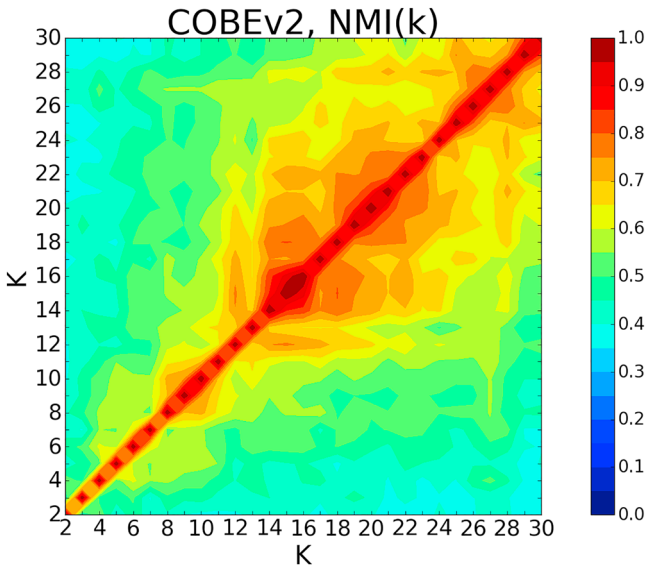

Figure A1. Normalized mututal information and its dependency on the K parameter for COBEv2.

estimated as

$$\mathrm{Var}[r_{i,j}] = \frac{1}{T}\sum_{\tau=-T}^{T} r_{i,i}(\tau) r_{j,j}(\tau), \tag{A1}$$

where T is the length of the time series and $r_{i,i}(\tau)$ the autocorrelation of the time series of grid cell i at lag τ. The scaled values $z_{i,j} = \frac{r_{i,j}}{\sqrt{\mathrm{Var}[r_{i,j}]}}$ approximately follow a standard normal distribution. Thus, significant cross correlations can be found applying a one-sided z test for a given level of significance α. In this work we always set $\alpha = 0.01$.

The threshold δ is then chosen to be the average of all significant correlations. Intuitively, a domain is a set of spatially contiguous grid cells and therefore the minimum degree of homogeneity has to be greater than the mean significant correlation of a set of randomly picked grid cells. δ depends on the significance level α, the autocorrelation structure of the time series and the correlation distribution of the field under study.

Appendix B: Adjacency Matrix of a Network Between Functional Domains and netCorr Metric: A Simple Example

The netCorr metric is computed as a two-dimensional correlation between the adjacency matrices of two networks. Differently from common approaches in the network science literature (Barabási, 2016; Newman, 2010), in our framework the entities of the system are not point-like structures but functional domains. The sizes, shapes, and number of these spatially embedded structures depend on the data set under investigation. Therefore, encoding their network in an adjacency matrix comparable across data sets is a nontrivial procedure. Using synthetic data, here we elucidate the steps to construct such a matrix.

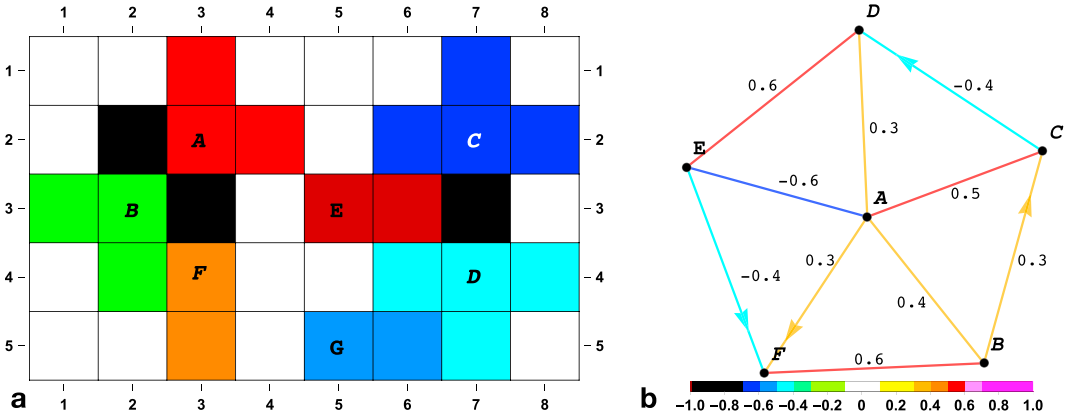

Figure B1. (a) Six domains on a spatial grid. Domains overlapping are shown in black. (b) The functional network between domains. Links colors indicate the corresponding cross correlations, arrows indicate temporal ordering of the interactions. Given the limited size of the network we also report all cross correlations.

Table B1
Domains' Coordinates and Strengths

Domain	(Row, column)	Strength
A	((1,3), (2,2), (2,3), (2,4), (3,3))	$s_N(A) = 2.25$
B	((2,2), (3,1), (3,2), (3,3), (4,2))	$s_N(B) = 1.35$
F	((3,3),(4,3),(5,3))	$s_N(F) = 1.35$
C	((1,7),(2,6),(2,7),(2,8),(3,7))	$s_N(C) = 1.3$
E	((3,5),(3,6),(3,7))	$s_N(E) = 1.6$
D	((3,7),(4,6),(4,7),(4,8),(5,7))	$s_N(D) = 1.35$
G	((5,5),(5,6))	$s_N(G) = 0$

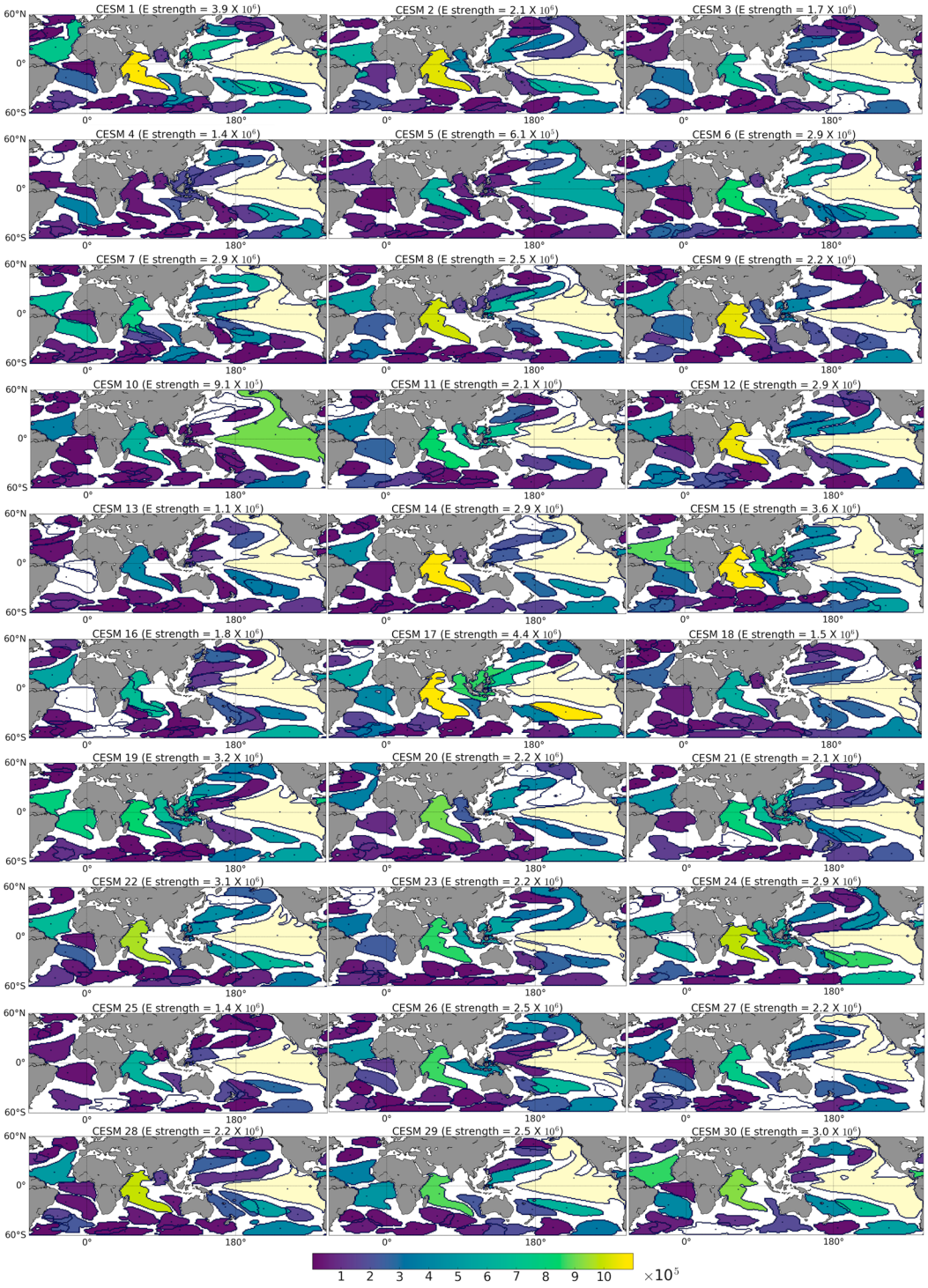

Figure C1. Strength maps for 30 members of the CESM-LE. The *E* strengths are indicated atop of each panel. Networks were computed after removing the individual trend to each member. CESM-LE = Community Earth System Model Large Ensemble.

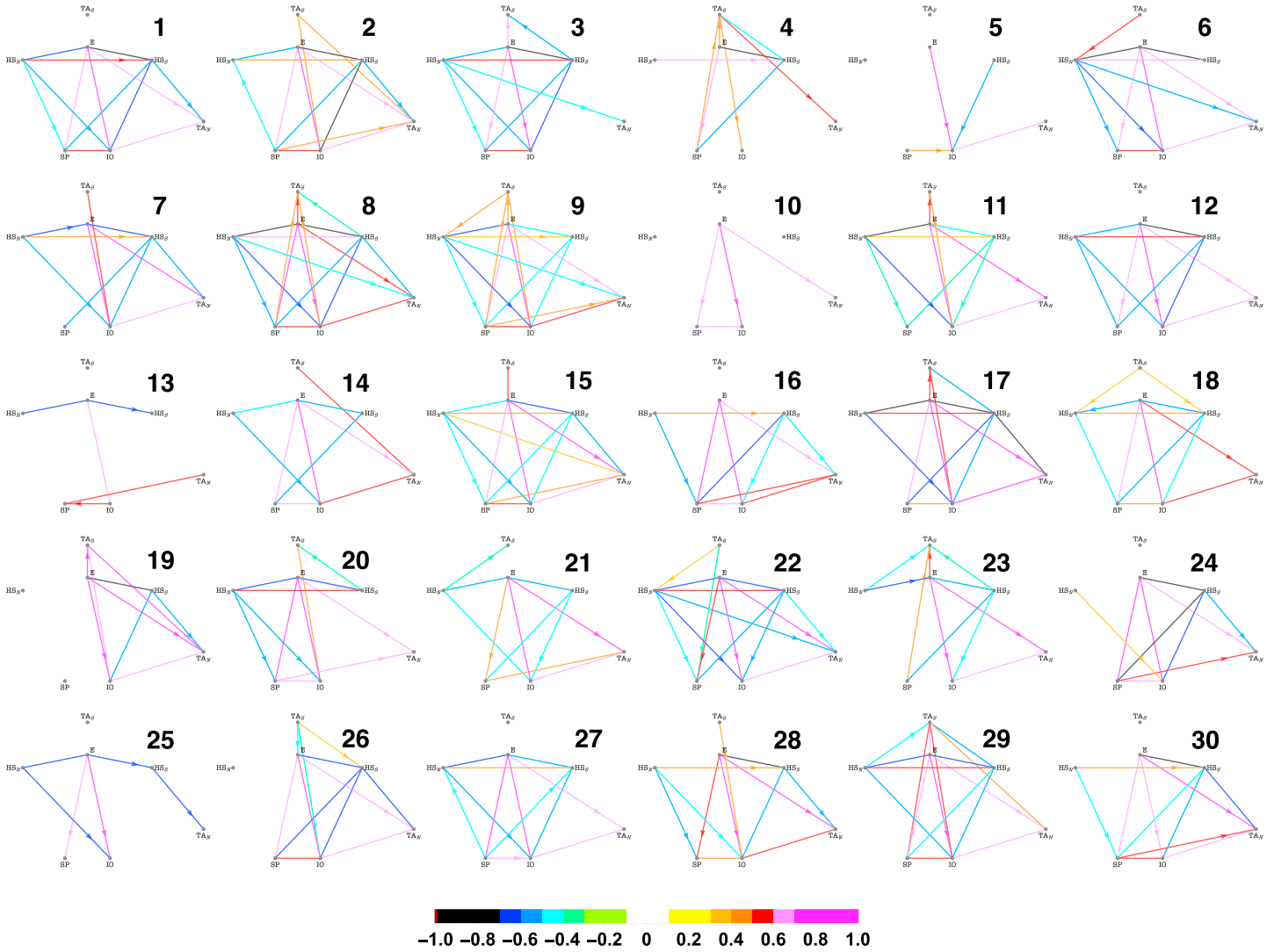

Figure C2. Networks identified between seven strong domains in 30 members of the CESM-LE. Link colors indicate the corresponding cross correlations and the arrows indicate the link directionalities. The lag ranges associated with some connections are reported. The networks were computed after removing the individual trend to each member. CESM-LE = Community Earth System Model Large Ensemble.

We consider six domains on a 8×5 spatial grid. Domains and their functional network N are shown in Figure B1. For clarity, all grid points belonging to each domain d_i along with domain strength $s_N(d_i)$ are shown in Table B1.

The number of nonmasked grid points is $n = 40$. For each of the n cells in the grid, we want to generate a n dimensional vector encoding the links of the domain it belongs to. This results in the computation of an adjacency matrix M_N of n rows and n columns.

It is useful to assign a label to every grid point (i, j) and use these labels as indices (k, l) of the adjacency matrix. For instance, label $k = 1$ corresponds to the grid point with coordinates $(1, 1)$, $k = 2$ to point $(1, 2)$, $k = 9$ to point $(2, 1)$, and so on until the last, $k = 40$, in position $(5, 8)$.

We consider each k and compute the adjacency matrix following instructions in section 2.2.4. Here we focus on few specific grid points and explain how to apply the rules described in section 2.2.4.

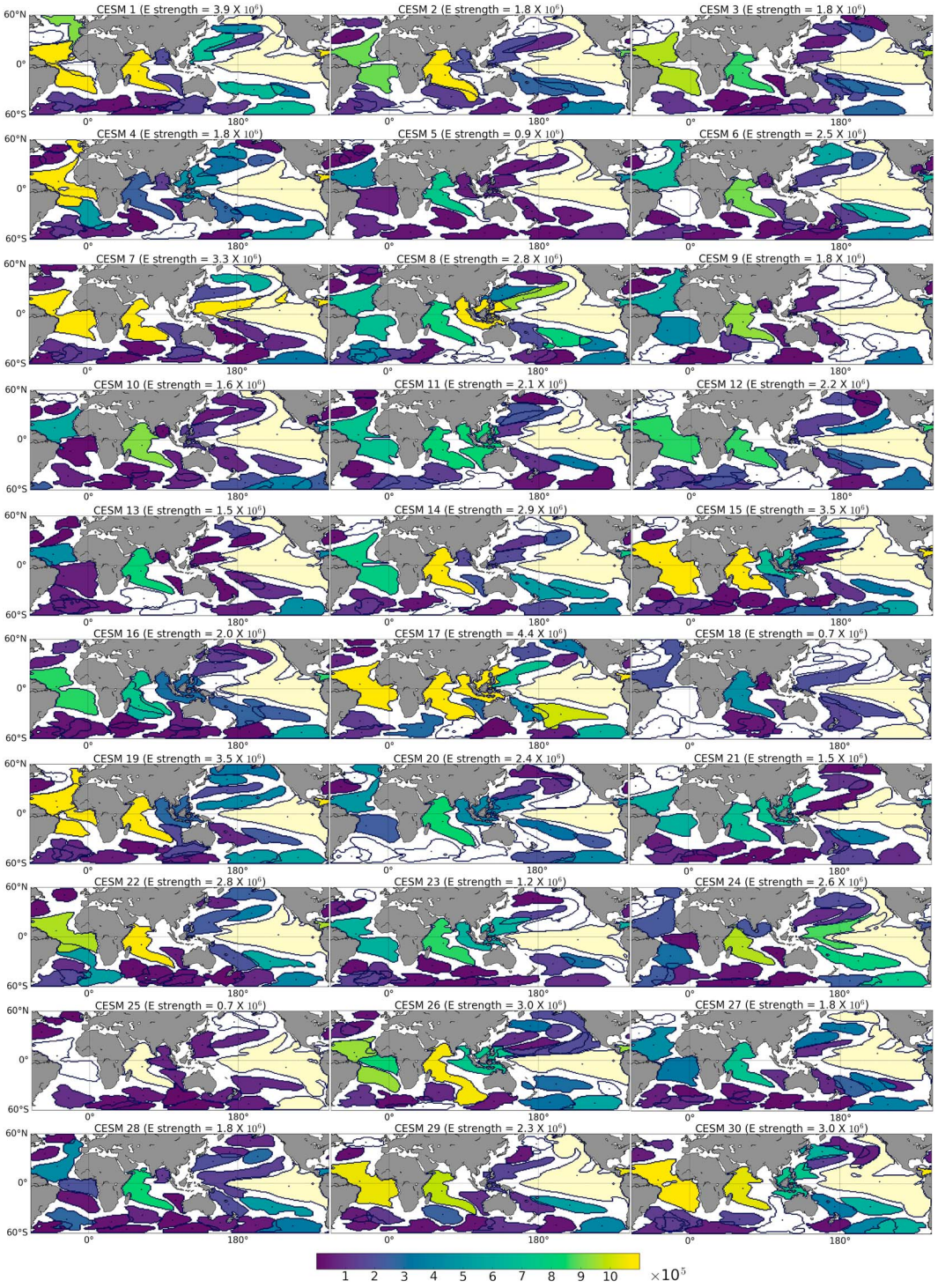

Figure C3. Strength maps for 30 members of the CESM-LE. The *E* strengths are indicated atop of each panel. Networks were computed after removing the ensemble trend to each member. CESM-LE = Community Earth System Model Large Ensemble.

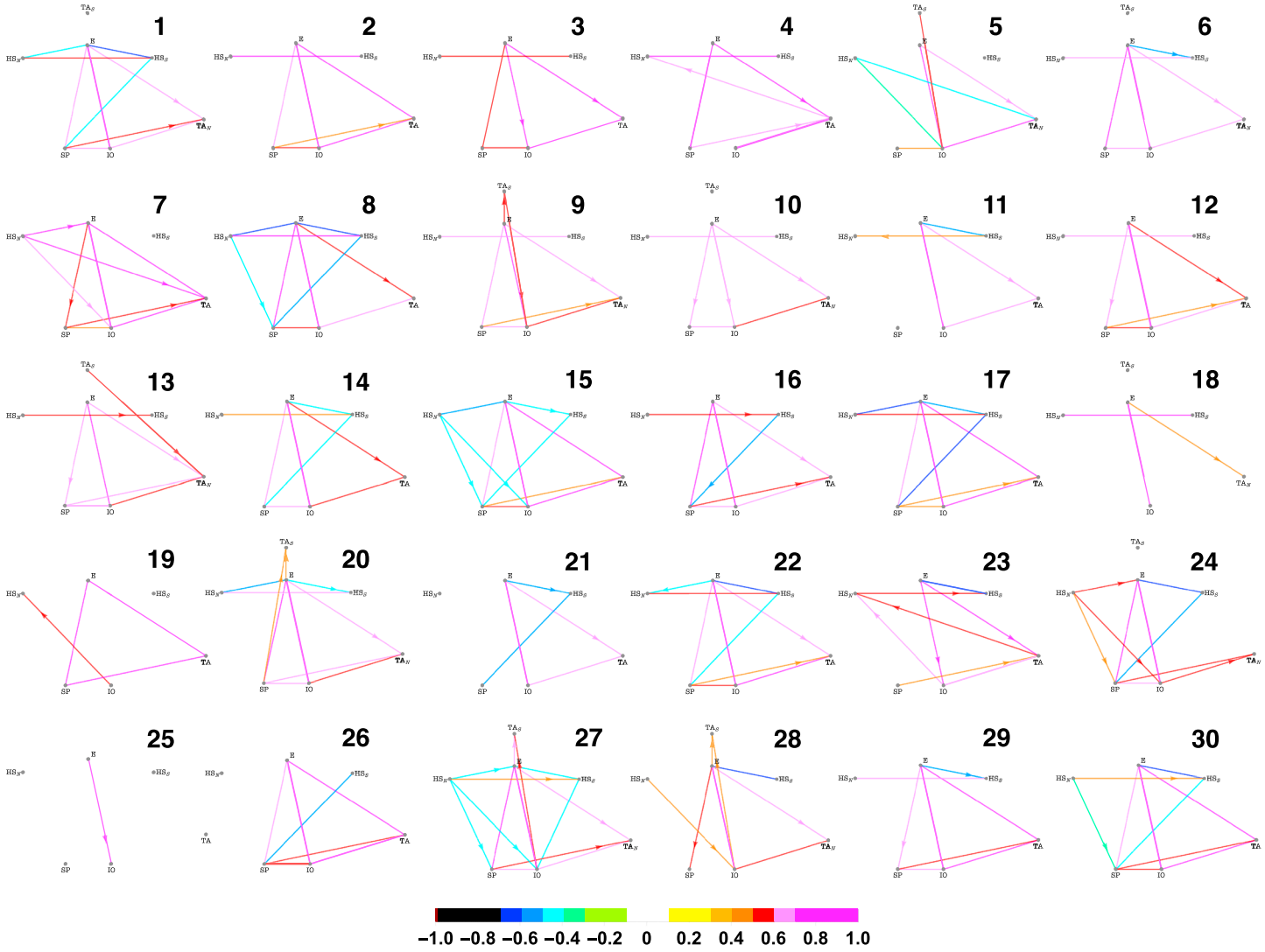

Figure C4. Networks identified between strong domains in 30 members of the CESM-LE. Link colors indicate the corresponding cross-correlations and the arrows indicate the link directionalities. The lag ranges associated with some connections are reported. The networks were computed after removing the ensemble trend to each member. CESM-LE = Community Earth System Model Large Ensemble.

We can group grid points k in two main categories:

1. k does not belong to any domain. In this case, a value of zero has to be set to all n entries in the kth row of M_N. For example $k = 1$ does not belong to any domain and its contribution to the connectivity pattern of the system is zero. All n entries in the first row of this adjacency matrix will be set equal to zero, and similarly for $k = 1, 2, 4, 5, 6, 8, 9, 13, 20, 24, 25, 28, 29, 33, 34, 36$, and 40. Additionally, if k belongs to a domain with zero strength, it also does not have a role in the connectivity pattern of the system. This is the case of $k = 37$ and $k = 38$, which belong to domain G with strength $s_N(G) = 0$ (see Table B1). All n entries of rows 37 and 38 in the adjacency matrix are set to zero.
2. k belongs to a domain d_i with strength $s_N(d_i) > 0$, as in the case $k = 7$. This k belongs to domain C. The 7th row of the adjacency matrix is computed as follows:

- All entries l that do not belong to any domain are set to zero. These entries are $l = 1, 2, 4, 5, 6, 8, 9, 13, 20, 24, 25, 28, 29, 33, 34, 36$, and 40.
- All entries l that belong to domains not connected to C are set to zero. These entries are $l = 21, 22, 27$, and 35.

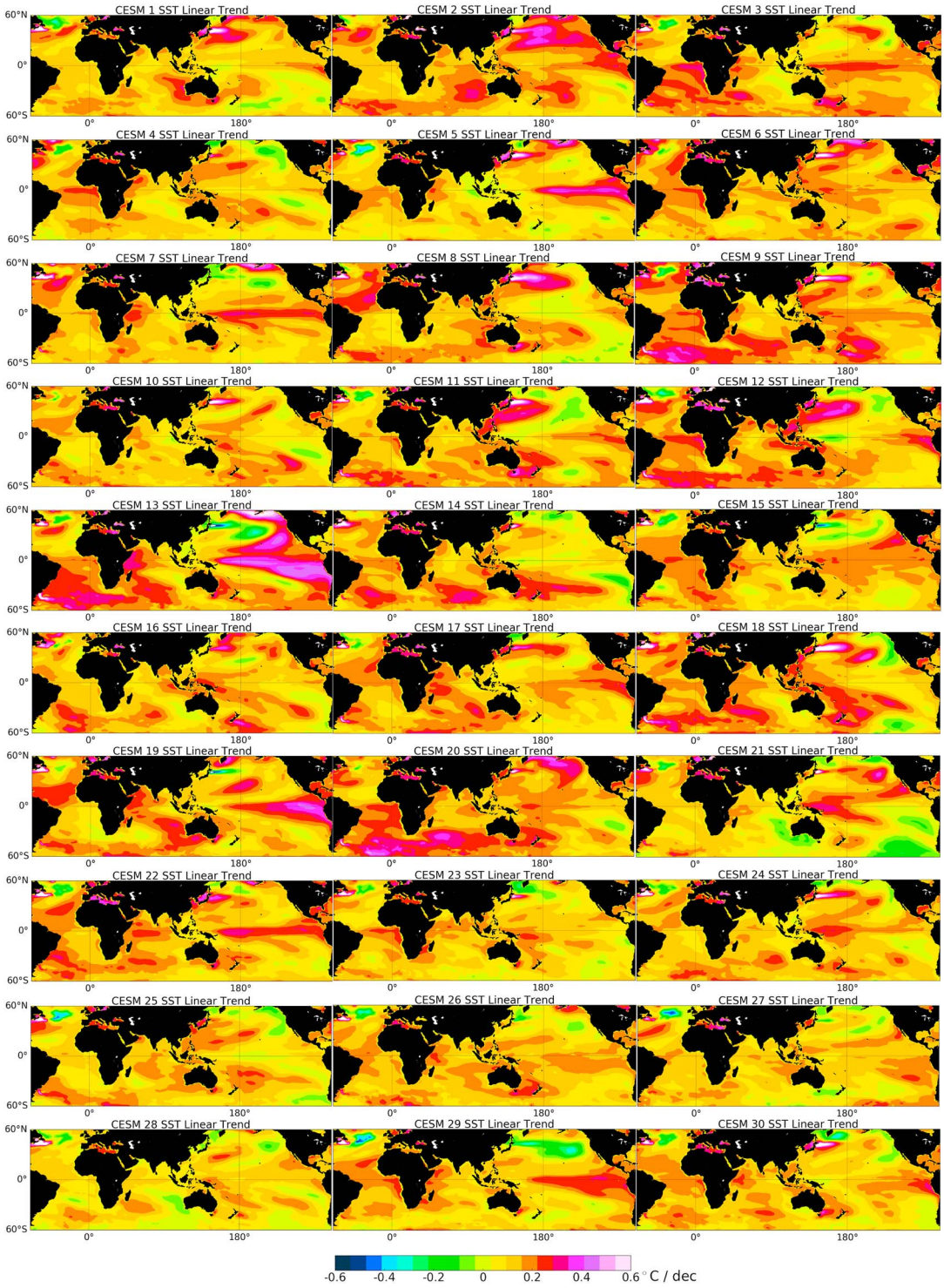

Figure D1. Linear trends of 30 members of the CESM-LE (Community Earth System Model Large Ensemble).

- All entries l that belong exclusively to domain C are set to zero (given that self loops are excluded in our framework). These entries are $l = 7, 14, 15$, and 16.
- If l belongs to a domain d_j connected to C with a correlation $r^*_{C,j}$, the value of $r^*_{C,j}$ is assigned to the l entry if C is leading d_j or if their lag range include zero. Because of this choice, entries $l = 17, 18$, and 26 in this row are set to zero even if these points belong to domain B connected with C. In the case of d_j overlapping

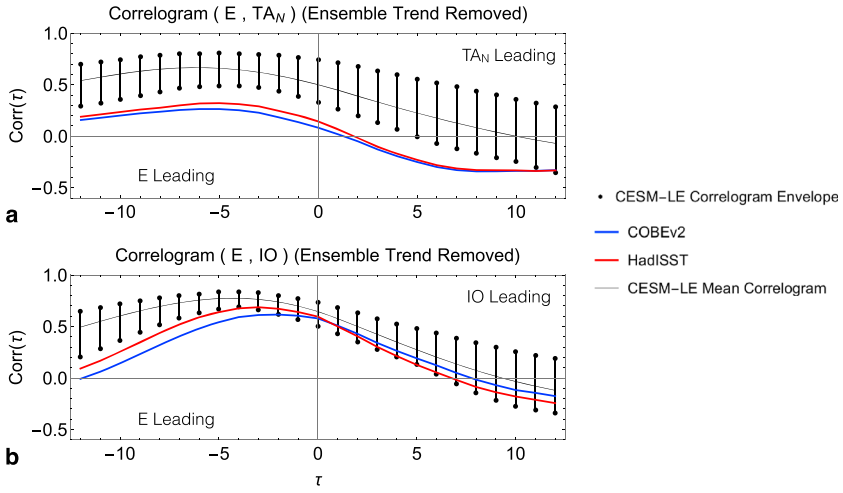

Figure E1. Correlograms between the E and TA_N (a) and IO (b) domains whenever the ensemble trend is removed. CESM-LE = Community Earth System Model Large Ensemble.

with other domains, the value that maximizes $|r^*_{C,j}|$ is chosen. For $k = 7$ an additional test would have to be performed for entries $l = 10$ and $l = 19$ that coincide with the overlapping of domains A and B, both connected with C. In this case $|r^*_{C,A}| > |r^*_{C,B}|$ so that entries $l = 10$ and $l = 19$ in the seventh row of the adjacency matrix should encode values of $r^*_{C,A}$. Similarly, the overlapping entry $l = 23$ is set equal to $r^*_{C,D}$.

- Finally, in point $k = 23$ (coordinates (3,7)) there is the overlapping of three domains (see Table B1). When filling row 23 of the adjacency matrix, this point is considered as part of the strongest domain E (see Table B1) and then treated as in the case $k = 7$.

Given two networks N_1 and N_2, and their adjacency matrices M_{N_1} and M_{N_2} the netCorr metric is given by the two-dimensional correlation of the two matrices. The two-dimensional correlation is computed in two steps: first the two n by n matrices are cast in two vectors of dimension n^2, and then a correlation between these two vectors is computed.

Appendix C: Modeled Networks

Strength maps and networks for all the 30 members of the CESM-LE are reported here, both in the case of individual trend (Figures C1 and C2) and ensemble trend removal (Figures C3 and C4).

Appendix D: Trends

Linear trends of all the 30 members analyzed are reported here in Figure D1.

Appendix E: Correlograms E–TA_N and E–IO Whenever the Ensemble Trend is Removed

Correlograms between the E and TA_N (Figure E1a) and IO (Figure E1b) domains whenever the ensemble trend is removed are reported here.

Appendix F: Autocorrelations of the E, TA_N, and IO Signals Whenever the Ensemble Trend is Removed

Autocorrelations of the E (Figure F1a), TA_N (Figure F1b), and IO (Figure F1c) signals whenever the ensemble trend is removed are reported here.

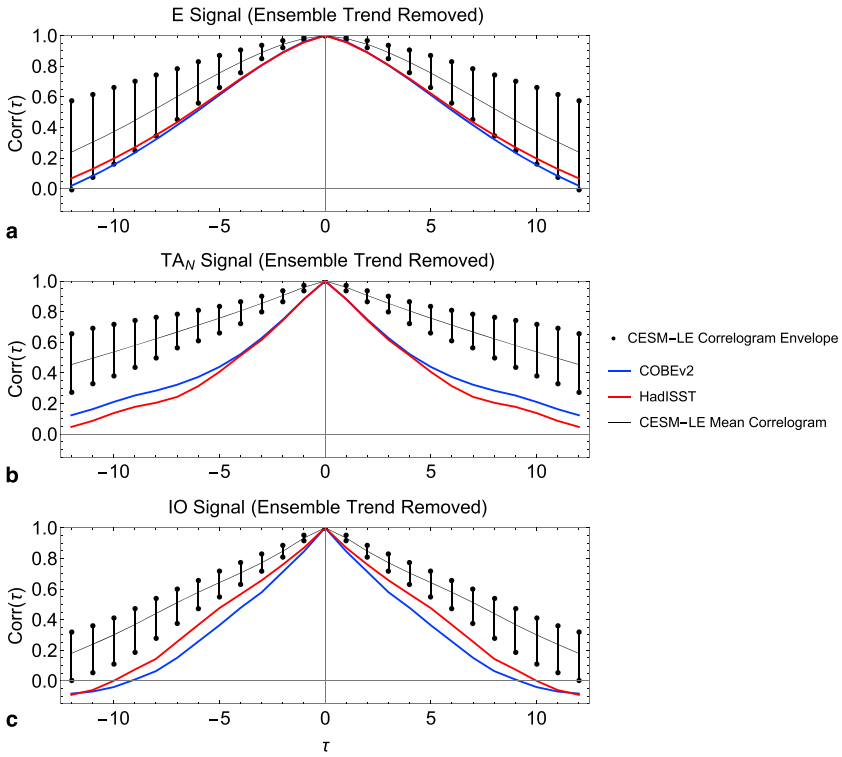

Figure F1. Autocorrelations of the *E* (a), TA_N (b), and *IO* (c) signals whenever the ensemble trend is removed. CESM-LE = Community Earth System Model Large Ensemble.

Acknowledgments
A. N. and F. F. received support from the Department of Energy (grant DE-SC0007145) and from the NASA MAP program (grant NNX13AP63G). We thank three anonymous reviewers for their comments that greatly improved the manuscript. We would like to thank Constantine Dovrolis for his important contributions to this project. F. F. acknowledges interesting and helpful discussions with Sebastián Ortega and Slawa Kabanovic.

References

Alexander, M. A. (2002). The atmospheric bridge: The influence of ENSO teleconnections on air-sea interaction over the global oceans. *Journal of Climate*, *15*, 2205–2228.
Baldassano, C., Beck, D. M., & Fei-Fei, L. (2015). Parcellating connectivity in spatial maps. *PeerJ*, *3*, 784.
Barabási, A. L. (2016). *Network science*. Cambridge, UK: Cambridge University Press.
Berezin, Y., Gozolchiani, A., Guez, O., & Havlin, S. (2012). Stability of climate networks with time. *Scientific Report*, *2*, 1–8. https://doi.org/10.1038/srep00666
Blumensath, T., Behrens, T. E., & Smith S. M. (2012). Resting-state fMRI single subject cortical parcellation based on region growing. International Conference on Medical Image Computing and Computer-Assisted Intervention, 2012:188áAS195.
Box, G. E., Jenkins, G. M., & Reinsel, G. C. (2011). *Time series analysis: Forecasting and control* (Vol. 734). CA, USA: John Wiley.
Bracco, A., Falasca, F., Nenes, A., Fountalis, I., & Dovrolis, C. (2018). Advancing climate science with knowledge discovery through mining. *Climate and Atmospheric Science*, *1*, 4. https://doi.org/10.1038/s41612-017-0006-4
Cai, W., & Cowan, T. (2013). Why is the amplitude of the Indian Ocean Dipole overly large in CMIP3 and CMIP5 climate models. *Geophysical Research Letters*, *40*, 1200–1205. https://doi.org/10.1002/grl.50208
Chiang, J. C. H., & Lintner, B. R. (2005). Mechanisms of remote tropical surface warming during El Niño. *Journal of Climate*, *18*, 4130–4149.
Chiang, J. C. H., & Sobel, A. H. (2002). Tropical tropospheric temperature variations caused by ENSO and their influence on the remote tropical climate. *Journal of Climate*, *15*, 2616–2631.
Chowdary, J. S., & Gnanaseelan, C. (2007). Basin-wide warming of the Indian Ocean during El Niño and Indian Ocean dipole years. *International Journal Of Climatology*, *27*, 1421–1438. https://doi.org/10.1002/joc.1482
Clauset, A., Newman, M. E. J., & Moore, C. (2004). Finding community structure in very large networks. *Physical Review E*, 066111, *70*.
Craddock, R. C., James, G. A., Holtzheimer, P. E., Hu, X., & Mayberg, H. S. (2012). A whole brain fMRI atlas generated via spatially constrained spectral clustering. *Human Brain Mapping*, *33*(8), 1914–1928.
Dai, A., Fyfe, J. C., Xie, S.-P., & Dai, X. (2015). Decadal modulation of global surface temperature by internal climate variability. *Nature Climate Change*, *5*, 555–559.
Deser, C., Phillips, A., Bourdette, V., & Teng, H. (2012). Uncertainty in climate change projections: The role of internal variability. *Climate Dynamics*, *38*, 527–547.
Ding, H., Keenlyside, N. S., & Latif, M. (2012). Impact of the Equatorial Atlantic on the El Niño Southern Oscillation. *Climate Dynamics*, *38*(9-10), 1965–1972. https://doi.org/10.1007/s00382-011-1097-y
Dommenget, D., & Latif, M. (2002). A cautionary note on the interpretation of EOFs. *Journal of Climate*, *15*, 216–225.
Dong, L., & Zhou, T. (2014). The formation of the recent cooling in the eastern tropical Pacific Ocean and the associated climate impacts: A competition of global warming, IPO, and AMO. *Journal of Geophysical Research: Atmospheres*, *119*, 11,272–11,287. https://doi.org/10.1002/2013JD021395
Donges, J. F., Zou, Y., Marwan, N., & Kurths, J. (2009a). The backbone of the climate network. *Europhysics Letters*, *87*, 48007.

Donges, J. F., Zou, Y., Marwan, N., & Kurths, J. (2009b). Complex networks in climate dynamics. *Europhysics Letters*, *174*, 157–179. https://doi.org/10.1140/epjst/e2009-01098-2

Drijfhout, S., van Oldenborgh, G. J., & Cimatoribus, A. (2012). Is a decline of AMOC causing the warming hole above the North Atlantic in observed and modeled warming patterns? *Journal of Climate*, *25*, 8373–8379. https://doi.org/10.1175/JCLI-D-12-00490.1

Ebert-Uphoff, I., & Deng, Y. (2017). Causal discovery in the geosciences—Using synthetic data to learn how to interpret results. *Computers & Geosciences*, *99*, 50–60.

England, M. H., McGregor, S., Spence, P., Meehl, G. A., Timmermann, A., Cai, W., et al. (2014). Recent intensification of wind-driven circulation in the Pacific and the ongoing warming hiatus. *Nature Climate Change*, *4*, 222–227.

Fayyad, U. M., Piatetsky-Shapiro, G., & Smyth, P. (1996). From data mining to knowledge discovery in databases. *Ai Magazine*, *17*(3), 37–54. https://doi.org/10.1609/aimag.v17i3.1230

Feldhoff, J. H., Lange, S., Volkholz, J., Donges, J. F., Kurths, J., & Gerstengarbe, F. W. (2014). Complex networks for climate model evaluation with application to statistical versus dynamical modeling of South American climate. *Climate Dynamics*, *44*, 1567–1581. https://doi.org/10.1007/s00382-014-2182-9

Feng, Q. Y., & Dijkstra, H. E. (2016). Climate network stability measures of El Niño variability. *Chaos*, *27*, 035801. https://doi.org/10.1063/1.4971784

Fountalis, I., Bracco, A., & Dovrolis, C. (2014). Spatio-temporal network analysis for studying climate patterns. *Climate Dynamics*, *42*, 879–899.

Fountalis, I., Bracco, A., & Dovrolis, C. (2015). ENSO in CMIP5 simulations: Network connectivity from the recent past to the twenty-third century. *Climate Dynamics*, *45*, 511–538.

Fountalis, I., Dovrolis, C., Bracco, A., Dilkina, B., & Keilholz, S. (2018). δ-MAPS: From spatio-temporal data to a weighted and lagged network between functional domains. *Applied Network Science*, *3*, 21. https://doi.org/10.1007/s41109-018-0078-z

Gill, A. E. (1980). Some simple solutions for heat-induced tropical circulations. *Quarterly Journal of the Royal Meteorological Society*, *106*, 447–462.

Granger, C. W. (1969). Investigating causal relations by econometric models and cross-spectral methods. *Econometrica*, *37*, 424–438.

Guez, O. C., Gozolchiani, A., & Havlin, S. (2014). Influence of autocorrelation on the topology of the climate network. *Physical Review E*, *90*(062814).

Ham, Y. G., Kug, J. S., Park, J. Y., & Jin, F. F. (2013). Sea surface temperature in the north tropical Atlantic as a trigger for El Niño/Southern Oscillation events. *Nature Geoscience*, *6*, 112–116.

He, J., Deser, C., & Soden, B. J. (2017). Atmospheric and oceanic origins of tropical precipitation variability. *Journal of Climate*, *30*, 3197–3217. https://doi.org/10.1175/JCLI-D-16-0714.1

Heuvel, M. V. D., Mandl, R., & Pol, H. H. (2008). Normalized cut group clustering of resting-state fMRI data. *PloS ONE*, *3*(4), 2001.

Hirahara, S., Ishii, M., & Fukuda, Y. (2014). Centennial-scale sea surface temperature analysis and its uncertainty. *Journal of Climate*, *27*, 57–75.

Hlinka, J., Jajcay, N., Hartman, D., & Paluš, M. (2017). Smooth information flow in temperature climate network reflects mass transport. *Chaos*, *27*(035811).

Hubert, L., & Arabie, P. (1985). Comparing partitions. *Journal of Classification*, *2*, 193–218.

Kaufmann, R. K., Kauppi, H., Mann, M. L., & Stock, J. H. (2011). Reconciling anthropogenic climate change with observed temperature 1998–2008. *Proceedings of the National Academy of Sciences*, *108*, 11,790–11,793.

Kawale, J., Chatterjee, S., Ormsby, D., Steinhaeuser, K., Liess, S., & Kumar, V. (2012). Testing the significance of spatio-temporal teleconnection patterns. Paper presented at the 18th ACM SIGKDD International Conference on Knowledge Discovery and Data Mining, Beijing, China, 12–16, 642–650.

Kawale, J., Liess, S., Kumar, A., Steinbach, M., Ganguly, A., Samatova, N. F., et al. (2011). Data guided discovery of dynamic climate dipoles. In *Conference on Intelligent Data Understanding*, United States, pp. 1–15.

Kawale, J., Liess, S., Kumar, A., Steinbach, M., Snyder, P., Kumar, V., et al. (2013). A graph-based approach to find teleconnections in climate data. *Statistical Analysis and Data Mining*, *6*(3), 158–179.

Kay, J. E., Deser, C., Phillips, A., Mai, A., Hannay, C., Strand, G., et al. (2015). The Community Earth System Model (CESM) large ensemble project. A community resource for studying climate change in the presence of internal climate variability. *Bulletin of the American Meteorological Society*, *96*, 1333–1349. https://doi.org/10.1175/BAMS-D-13-00255.1

Keenlyside, N. S., & Latif, M. (2007). Understanding equatorial Atlantic interannual variability. *Journal of Climate*, *20*(1), 131–142.

Kittel, T., Ciemer, C., Lotfi, N., Peron, T., Rodrigues, F., Kurths, J., & Donner, R. V. (2017). Global teleconnectivity structures of the El Niño–Southern Oscillation and large volcanic eruptions—An evolving network perspective. *Nonlinear Processes in Geophysics Discussions*. https://doi.org/10.5194/npg-2017-69

Klein, S. A., Soden, B. J., & Lau, N. C. (1999). Remote sea surface temperature variations during ENSO: Evidence for a tropical atmospheric bridge. *Journal of Climate*, *12*(4), 917932.

Kosaka, Y., & Xie, S.-P. (2013). Recent global-warming hiatus tied to equatorial Pacific surface cooling. *Nature*, *501*, 403–407.

Lancichinetti, A., Fortunato, S., & Kertész, J. (2009). Detecting the overlapping and hierarchical community structure in complex networks. *New Journal of Physics*, *11*, 033015.

Liguori, G., & Di Lorenzo, E. (2018). Meridional modes and increasing pacific decadal variability under greenhouse forcing. *Geophysical Research Letters*, *45*, 983–991. https://doi.org/10.1002/2017GL076548

Lockwood, M. (2008). Recent changes in solar outputs and the global mean surface temperature. III. Analysis of contributions to global mean air surface temperature rise. *Proceedings of the National Academy of Sciences*, *464*, 1387–1404.

Lu, Y., Jiang, T., & Zang, Y. (2003). Region growing method for the analysis of functional MRI data. *NeuroImage*, *20*(1), 455–465.

Ludescher, J., Gozolchiani, A., Bogachev, M. I., Bunde, A., Havlin, S., & Schellnhuber, H. J (2013). Improved El Niño forecasting by cooperativity detection. *Proceedings of the National Academy of Sciences*, *110*(29), 11742–11745. https://doi.org/10.1073/pnas.1317354110

Maher, N., Matei, D., Milinski, S., & Marotzke, J. (2018). ENSO change in climate projections: Forced response or internal variability? *Geophysical Research Letters*, *45*, 11,390–11,398. https://doi.org/10.1029/2018GL079764

Mann, M. E., Steinman, B. A., & Miller, S. K. (2014). On forced temperature changes, internal variability, and the AMO. *Geophysical Research Letters*, *41*, 3211–3219. https://doi.org/10.1002/2014GL059233

Martín-Rey, M., Rodríguez-Fonseca, B., Polo, I., & Kucharski, F. (2014). On the Atlantic-Pacific Niños connection: A multidecadal modulated mode. *Climate Dynamics*, *43*, 3163–3178. https://doi.org/10.1007/s00382-014-2305-3

Matsuno, T. (1966). Quasi-geostrophic motions in the equatorial area. *Quarterly Journal of the Royal Meteorological Society*, *44*, 25–43.

McDaid, A. F., Greene, D., & Hurley, N. (2013). Normalized mutual information to evaluate overlapping community finding algorithms. preprintarXiv:1110.2515.

Medhaug, I., Stolpe, M. B., Fischer, E. M., & Knutti, R. (2017). Reconciling controversies about the 'global warming hiatus'. *Nature*, *545*, 41–47. https://doi.org/10.1038/nature22315

Molod, A., Takacs, L., Suarez, M., & Bacmeister, J. (2015). Development of the GEOS-5 atmospheric general circulation model: Evolution from MERRA to MERRA2. *Geoscientific Model Development*, *8*, 1339–1356.

Newman, M. (2010). *Networks: An introduction*. Oxford, UK: Oxford University Press.

Radebach, A., Donner, R. V., Runge, J., Donges, J. F., & Kurths, J. (2013). Disentangling different types of El Niño episodes by evolving climate network analysis. *Physical Review E*, *88*, 052807. https://doi.org/10.1103/PhysRevE.88.052807

Rahmstorf, S., Box, J. E., Feulner, G., Mann, M. E., Alexander, R., Rutherford, S., & Schaffernicht, E. J. (2015). Exceptional twentieth-century slowdown in Atlantic Ocean overturning circulation. *Nature Climate Change*, *5*, 475–480.

Rayner, N. A., Parker, D. E., Horton, E. B., Folland, C. K., Alexander, L. V., Rowell, D. P., et al. (2003). Global analyses of sea surface temperature, sea ice, and night marine air temperature since the late nineteenth century. *Journal of Geophysical Research*, *108*(D14), 4407. https://doi.org/10.1029/2002JD002670

Regayre, L. A., Pringle, K. J., Booth, B. B. B., Lee, L. A., Mann, G. W., Browse, J., et al. (2014). Uncertainty in the magnitude of aerosol-cloud radiative forcing over recent decades. *Geophysical Research Letters*, *41*, 9040–9049. https://doi.org/10.1002/2014GL062029

Rodríguez-Fonseca, B., Polo, I., García-Serrano, J., Losada, T., Mohino, E., Mechoso, C. R., & Kucharski, F. (2009). Are Atlantic Niños enhancing Pacific ENSO events in recent decades. *Geophysical Research Letters*, *36*, L20705. https://doi.org/10.1029/2009GL040048

Rodriguez-Fonseca, B., Polo, I., Garcia-Serrano, J., Losada, T., Mohino, E., Mechoso, C. R., & Kucharski F. (2009). Are Atlantic Ninos enhancing Pacific ENSO events in recent decades? *Geophysical Research Letters*, *36*, L20705. https://doi.org/10.1029/2009GL040048

Runge, J., Petoukhov, V., Donges, J. F., Hlinka, J., Jajcay, N., Vejmelka, M., et al. (2015). Identifying causal gateways and mediators in complex spatio-temporal systems. *Nature Communications*, *6*, 8502.

Saravanan, R., & Chang, P. (1999). Interactions between tropical Atlantic variability and El Niño Southern Oscillation. *Journal of Climate*, *13*, 2177–2194.

Steinhaeuser, K., Chawla, N. V., & Ganguly A. R. (2010). An exploration of climate data using complex networks. Paper presented at the 16th ACM SIGKDD international conference on Knowledge discovery and data mining, 12:25-32.

Steinhaeuser, K., Ganguly, A. R., & Chawla, N. V. (2012). Multivariate and multiscale dependence in the global climate system revealed through complex networks. *Climate Dynamics*, *39*(3-4), 889–895.

Steinhaeuser, K., & Tsonis, A. A. (2014). A climate model intercomparison at the dynamics level. *Climate Dynamics*, *42*, 1665–1670. https://doi.org/10.1007/s00382-013-1761-5

Swanson, K. L., & Tsonis, A. A. (2009). Has the climate recently shifted? *Geophys Research Letters*, *36*, L06711. https://doi.org/10.1029/2008GL037022

Tantet, A., & Dijkstra, H. A. (2014). An interaction network perspective on the relation between patterns of sea surface temperature variability and global mean surface temperature. *Earth System Dynamics*, *5*, 1–14. https://doi.org/10.5194/esd-5-1-2014

Thirion, B., Varoquaux, G., Dohmatob, E., & Poline, J.-B. (2014). Which fMRI clustering gives good brain parcellations? *Frontiers in Neuroscience*, *8*, 167.

Thorne, P., Outten, S., Bethke, I., & Seland, Ø. (2015). Investigating the recent apparent hiatus in surface temperature increases: 2. Comparison of model ensembles to observational estimates. *Journal of Geophysical Research: Atmospheres*, *120*, 8597–8620. https://doi.org/10.1002/2014JD022805

Tsonis, A. A., & Roebber, P. J. (2004). The architecture of the climate network. *Physica A*, *333*, 497–504.

Tsonis, A. A., Swanson, K., & Kravtsov, S. (2007). A new dynamical mechanism for major climate shifts. *Geophysical Research Letters*, *34*, L13705. https://doi.org/10.1029/2007GL030288

Tupikina, L., Rehfeld, K., Molkenthin, N., Stolbova, V., Mar-wan, N., & Kurths, J. (2014). Characterizing the evolution of climate networks. *Nonlinear Processes in Geophys*, *21*, 705–711. https://doi.org/10.5194/npg-21-705-2014

von Storch, H., & Zwiers, F. W. (2001). *Statistical analysis in climate research*. Cambridge: Cambridge University Press.

Wang, Y., Gozolchiani, A., Ashkenazy, Y., Berezin, Y., Guez, O., & Havlin, S. (2013). Dominant imprint of Rossby waves in the climate network. *Physical Review Letters*, *111*, 138501.

Wang, C., Lee, S. K., & Mechoso, C. R. (2010). Interhemispheric influence of the Atlantic warm pool on the southeastern Pacific. *Journal of Climate*, *23*(2), 404–418.

Wang, G., Swanson, K. L., & Tsonis, A. A. (2009). The pacemaker of major climate shifts. *Geophysical Research Letters*, *36*, L07708. https://doi.org/10.1029/2008GL03874

Yamasaki, K., Gozolchiani, A., & Havlin, S. (2008). Climate networks around the globe are significantly affected by El Niño. *Physical Review Letters*, *100*, 228501.

Yao, S.-L., Huang, G., Wu, R.-G., & Qu, X. (2016). The global warming hiatus-a natural product of interactions of a secular warming trend and a multi-decadal oscillation. *Theoretical and Applied Climatology*, *123*, 349–360.

Zebiak, S. E. (1586). Air-sea interaction in the equatorial Atlantic region. *Journal of Climate*, *6*, 1567–6.

Zheng, X. T., Hui, C., & Yeh, S. W. (2018). Response of ENSO amplitude to global warming in CESM large ensemble: uncertainty due to internal variability. *Climate Dynamics*, *50*, 4019. https://doi.org/10.1007/s00382-017-3859-7

Zhou, C., Zelinka, M. D., & Klein, S. A. (2016). Impact of decadal cloud variations on the Earth's energy budget. *Nature Geoscience*, *9*, 871–874.